Crystal plasticity simulation of strain aging phenomena in α-titanium at room temperature

CrossMark

Arina Marchenko, Matthieu Mazière*, Samuel Forest, Jean-Loup Strudel

Mines ParisTech, Centre des Matériaux, CNRS UMR 7633, BP 87, 91003 Evry Cedex, France

A B S T R A C T

Strain aging phenomena are shown to affect the viscoplastic behavior of commercially pure α-titanium at room temperature. A yield stress anomaly corresponding to static strain aging was experimentally observed when the material was loaded in the transverse direction. At low strain rates small serrations on the stress-strain curves, typical for the Portevin-Le Chatelier effect are observed for the material loaded in the transverse and rolling directions at room temperature. The presence of a stress peak is attributed to the interaction between activated <c+a> slip systems with the atoms of interstitial oxygen. The Portevin-Le Chatelier effect is presumably due to the non-planar core of screw-type dislocations. A phenomenological strain aging model is combined with a comprehensive description of slip systems active in HCP crystals in order to take into account the role of crystal plasticity in static as well as dynamic strain aging. Finite element simulations are performed on polycrystalline aggregates with various numbers of grains accounting for the elastic and plastic anisotropy of α-titanium. The simulations of static strain aging do not show formation and propagation of macroscopic shear bands. Instead, a complex strain localization phenomenon is taking place within some grains and specific associations of grains, which leads to the formation of meso-Lüders bands. The results of dynamic strain aging simulations predict the initiation and propagation of macroscopic Portevin-Le Chatelier bands even in the presence of positive apparent strain rate sensitivity.

© 2016 Elsevier Ltd. All rights reserved.

1. Introduction

High strength in combination with low density and good corrosion resistance make titanium (Ti) and its alloys widely used metals in aerospace, chemical and petrochemical industries. Among them, commercially pure (CP) α-Ti is of a great interest due to its high environmental resistance and good workability. Pure α-Ti has a hexagonal close-packed crystal structure with a c/a ratio of 1.586 at ambient temperature. Strong plastic anisotropy due to crystallographic texture and the possibility of twinning is responsible for the complexity of the deformation behavior of α-Ti. Three slip system families with Burgers vector of <a>-type $<\bar{2}110>$ gliding in basal (0001), prismatic $\{10\bar{1}0\}$ or first-order pyramidal $\{10\bar{1}1\}$ planes constitute a set of 12 slip systems including only 4 kinematically independent ones (see Fig. 1). Some additional *non* <a>-type deformation mechanisms such as pyramidal <c+a> dislocation slip and four twinning systems accommodate the plastic deformation along the c-axis (Lütjering and Williams, 2007). Prismatic <a> slip was found to be the easiest in CP-Ti, thus governing the
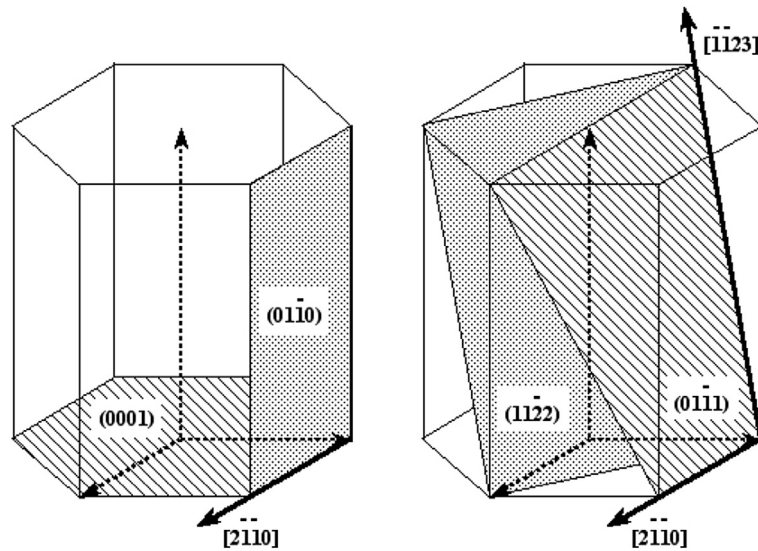
Fig. 1. Slip systems in α-titanium, after Guillot et al. (2001).

room-temperature plastic deformation. The relative ease of prismatic slip was explained by the lowest stacking fault energy for the <a>-dislocations associated with a non-planar dislocation core structure (Legrand, 1984).

A large number of studies devoted to the mechanical behavior of Ti has been conducted over the past few decades. In particular, the phenomena of dynamic and static strain aging and the underlying physical mechanisms have been the subjects of numerous investigations and of some long-standing debates.

Strain aging is usually associated with interactions between dislocations and point defects, i.e. vacancies, self-interstitials, substitutional and interstitial impurities. Solute atoms can migrate to dislocations and then segregate in or near their core, thus inhibiting the dislocation motion. In order to move the dislocation away from the solute rich regions, an extra stress is required to overcome attractive dislocation-defect interactions. At sufficiently high temperatures and/or low strain rates, the point defects can migrate back to dislocations, thus causing repeated locking—unlocking processes called dynamic strain aging (DSA). These intermittent and unstable localized strain bursts lead to the discontinuous yielding phenomenon known as Portevin-Le Chatelier (PLC) effect, characterized by serrations on the tensile stress-strain curve. At a given temperature and impurity concentration, the average flow stress needed to unpin dislocations, increases with decreasing strain rate or increasing waiting time of dislocations. As a result, the flow stress of the material vs. strain rate is decreasing and may even become negative, leading to the so-called negative strain rate sensitivity (NSRS), according to Kubin and Estrin (1991). When the imposed strain rate falls into the range of NSRS, the initiation and propagation of plastic strain rate localization bands in multiple sites of a specimen can be observed during the straining process (Hull and Bacon, 1984).

Static strain aging (SSA) is usually manifested by a marked yield point or a stress peak on the stress-strain curve when a prestrained specimen is unloaded and aged for a preset time and then reloaded. When dislocations cooperatively break away from their obstacles, strain localization bands called Lüders bands are formed at one site of the specimen and spread through the sample (Kubin et al., 1992).

Titanium and its alloys always contain some residual impurities such as nitrogen, oxygen, carbon, hydrogen. Rosi and Perkins (1953) were the first to report strain aging phenomena in CP Ti at elevated temperatures and they attributed it to the segregation of nitrogen atoms. According to Doner and Conrad (1973), pinning being controlled by diffusion, the activation energy of the process at the atomic scale is that for the diffusion of the solutes responsible for the pinning. The investigation of SSA in CP Ti at elevated temperatures by Donoso and Reed-Hill (1977) indicates that the activation energy of the process is in good agreement with that for the diffusion of oxygen in Ti. At intermediate and low temperatures, Conrad (1981) ascribed the yield peak in CP Ti to dislocation multiplication mechanisms. An alternative explanation of the yield peak in CP Ti observed at room temperature was recently proposed by Roth et al. (2014) who suggested that distinct slip systems have different strain-rate sensitivities. The tendency for the yield peak formation was explained by the initially dominant activity of pyramidal slip with a critical resolved shear stress (CRSS), resulting in a higher yield stress.

The significance of DSA in CP Ti at elevated temperatures was studied by Doner and Conrad (1973), Garde et al. (1972). They suggested that interstitial oxygen interacting with mobile dislocations through bulk diffusion can be responsible for DSA above 600 K, while DSA around 350 K might be due to hydrogen that has a higher diffusivity. According to Senkov and Jonas (1996), solute hydrogen reduces the extent of DSA in titanium at high temperatures by weakening the interaction between dislocations and impurity atoms thus causing material softening. Nemat-Nasser et al. (1999) argued that the activation

energies for volume diffusion of solute atoms may not be pertinent parameters to determine which solute is responsible for DSA in a given temperature range. He was the first who documented experimentally DSA of CP Ti near room temperature presumably caused by the pipe diffusion of interstitial atoms of oxygen along or inside the dislocation core.

Another mechanism based on the internal lattice friction was proposed to control the motion of screw <a> dislocations in Ti. The applied resolved shear stress required to make a dislocation glide in an otherwise perfect crystal is called the Peierls stress. It is a function of the dislocation core structure. The Peierls stress can substantially increase when the local concentration of solute atoms increases. It can also induce stress instabilities contributing to static and dynamic strain aging, according to Caillard and Martin (2003), Hull and Bacon (1984). Naka et al. (1991, 1988), Naka (1983) and Biget and Saada (1989) studied the importance of lattice friction in the low-temperature deformation of α Ti single crystals. *Post-mortem* transmission electron microscopic (TEM) observations exhibit a large density of long rectilinear screw <a> dislocations in the prismatic planes that govern room-temperature plastic deformation of α Ti. *In-situ* TEM deformation tests by Farenc et al. (1993, 1995) revealed a jerky motion of these dislocations with a series of sudden jumps between locked positions. It was concluded that the plastic flow of α Ti at room temperature is controlled by Peierls type frictional forces in connection with a non-planar core structure of the screw dislocations. According to the model of Couret and Caillard (1991), the dislocation takes alternately two configurations: a low energy, stable and sessile configuration with a core spread on several potential glide planes (Ghazisaeidi and Trinkle, 2012), and a high energy, metastable and glissile configuration with a core confined into a single glide plane (prismatic, pyramidal or basal) (Clouet, 2012). In this latter configuration, dislocation segments can jump over variable distances that can range from a single interatomic distance (classical Peierls mechanism) to large distances (locking-unlocking mechanism). Solute atoms of oxygen are expected to harden α Ti through a short range mechanical interaction in which the crystal distortions, introduced by the interstitial atoms, stabilize the core structure of screw dislocations. This results in a more difficult sessile-glissile transition and thus a larger lattice friction (Caillard and Martin, 2003). Transitions from one configuration to another being thermally activated, a decrease of the jump length and an increase in the jump frequency at higher temperature is observed experimentally by means of *in-situ* experiments. At low temperatures, the deformation is controlled by the locking-unlocking mechanism (Couret and Caillard, 1991). Long rectilinear segments of screw dislocations are observed and the activation parameters are those of the Friedel and Escaig model (Friedel, 1964; Escaig, 1968) (transition from a sessile to a glissile configuration before glide in the prismatic planes). At high temperatures, a large density of macrokink pairs is moving along bowed segments of dislocations and the kink pair mechanism (nucleation and mobility) is controlling plasticity (Farenc et al., 1995; Naka et al., 1988; Naka, 1983; Jousset, 2008).

Various constitutive models attempting to reproduce the SSA and DSA phenomena have been suggested in the literature. Two main types of these models are based on the physical origin of the strain aging, i.e. on dislocation-solute interaction. The first type of elastic-viscoplastic constitutive models proposed by Kubin and Estrin (Penning, 1972; Kubin and Estrin, 1985) accounts for an explicit mathematical description of strain rate sensitivity, which tends to zero or negative values of SRS in some range of strain rate and temperature when the PLC serrations are observed. Using such a phenomenological model in finite element (FE) code, the simulation of the propagation of the Lüders bands was implemented by several authors: Tsukahara and Iung (1998, 1999) in 2D plates; Kok et al. (2003) in 3D polycrystalline flat specimens; Benallal et al. (2006) in smooth and pre-notched axisymmetric tensile specimens. The second type of models initially proposed by McCormick (1988) and later improved by Mesarovic (1995), includes an internal variable t_a, called aging time, that controls the increase in the local solute concentration at temporarily arrested dislocations. This model class has been used in many recent PLC FE simulations (Zhang et al., 2001; Graff et al., 2004, 2005; Mazière et al., 2010; Colas et al., 2014; Marais et al., 2012) and more recently in Yu et al. (2012); Chaboche et al. (2013) for complex cyclic loading conditions. Some attempts to introduce crystal plasticity formulations into a multiscale modeling of the jerky flow in polycrystals were carried out by Kok et al. (2003) and later by Fressengeas et al. (2005). However, for the sake of simplicity, those models were not taking into account the strain and strain rate localization phenomena inside the grains.

In spite of the large number of studies devoted to the SSA and DSA in CP α-Ti, up to date no experimental evidence of macroscopic strain localization band nucleation and propagation at room temperature in CP α-Ti has been reported in the literature. In their recent work, Roth et al. (2014) reconstructed strain-rate patterns during the tensile deformation of the sample using a CCD camera. The observation of the evolution of the local strain rate at a millimeter scale showed no plastic front propagation. At the same time, as it was noticed by Efstathiou et al. (2010), the manifestation of deformations at one microscopic length scale may be different at larger length scales, especially for materials with inhomogeneous microstructure (Cho and Chasiotis, 2007). Héripré et al. (2007), studying local variations of plastic deformation in polycrystalline Zr by strain field mapping, reported strongly heterogeneous distributions of strain in relation with the underlying crystal grain orientations on a tensile specimen yet deforming homogeneously on the macro-scale. They concluded that for an accurate description of the mechanical properties of the material, it is necessary to account for the local microstructure and crystalline nature of the specimen at the grain scale in a polycrystalline aggregate. Many recent experimental and numerical investigations (Efstathiou et al., 2010; Héripré et al., 2007; Cho and Chasiotis, 2007; Raabe et al., 2001; Barbe et al., 2001a, b; Zhang et al., 2015) confirm that heterogeneous straining patterns and strain localization modes observed in materials with low symmetry crystal structure such as HCP α Ti, are correlated with their locally activated slip systems, the local texture and possibly the nature of the grain boundaries. Therefore, in α Ti a numerical model at finer scale (micrometer) taking into account the local arrangement of grains and a detailed description of their slip systems is necessary to understand the heterogeneities in strain field space and time distribution.

In the present study, we propose a new crystal plasticity formulation and perform FEM simulations in order to capture the strain aging phenomena at the grain scale within a polycrystal and the induced anisotropy of the mechanical properties of CP α-Ti. The novelty of this work consists in the development of a mesoscale strain aging model that enables the investigation of multiple slip activities taking place at the scale of a grain. It will be shown that these slip activities can lead to cooperative deformation modes inside the grains of a polycrystal causing the development of locally mobile plastic heterogeneities inside the material. This viscoplastic anisotropic model captures, at least qualitatively, the mesoscopic, as well as macroscopic responses of a material with low crystalline symmetry in a large range of plastic strain rates.

The present paper is organized as follows. In Section 2, experimental evidence of strain aging phenomena in CP α-Ti is reported. In Section 3 the constitutive equations of the model for both anomalous yield point and PLC effect are presented. An internal variable called the aging time t_a is i introduced in a crystal plasticity model to simulate the effect of strain aging. In Section 4, finite element (FE) simulations are performed on polycrystalline samples taking into account the effect of anisotropy of titanium in order to identify the parameters of the model. In Section 5, the model is shown to reproduce the anisotropic behavior and strain aging effect. The cooperative deformation modes in the polycrystal are evidenced. Finally, the dislocation-solute interactions, the frictional mechanisms and related questions are discussed.

2. Experimental methods and results

2.1. Materials and experimental procedures

In the present study CP α-Ti of Grade 2 and Grade 4 were investigated. The nominal chemical composition of the materials is given in Table 1. Cylindrical test pieces with a 8 mm diameter and 16 mm gauge length were extracted from cold-rolled plates and cut parallel (longitudinal direction LD) and perpendicular to the rolling direction (transverse direction TD) of the plates. The specimens were then annealed at 500 °C for 12 h under high vacuum.

The electron back-scattered diffraction (EBSD) analysis performed by Barkia (2014) showed that both materials have an equiaxed grain microstructure with an average grain size of 30 μm for Grade 2 and 42 μm for Grade 4, see Fig. 2 (a). The crystallographic texture of both grades has a $<10\bar{1}0>$ direction parallel to LD and $<c>$ axes tilted from 30 to 90° away from the normal direction (ND) towards the TD, see Fig. 2 (b,c), characters that correspond to the typical texture of the cold-rolled Ti sheet (Keeler and Geisler, 1957).

Tensile tests were performed at room temperature on both TD and LD cylindrical samples of Grade 2 and Grade 4 at a fixed strain rate of 2×10^{-4} s^{-1} and with tenfold upward and downward strain-rate jumps ranging from 2×10^{-6} s^{-1} to 2×10^{-2} s^{-1}. Additional *in-situ* tensile tests on flat TD and LD specimens, 1.2 mm thick, 6 mm wide and 25 mm long were carried out in a scanning electron microscope (SEM) in order to analyze the main deformation modes. The critical resolved shear stress (CRSS) for each slip system was estimated based on the slip trace analysis coupled with EBSD technique and TEM observations. More information about the techniques employed can be found in Barkia (2014), Barkia et al. (2015a). Prismatic slip with the lowest CRSS was found to be the predominant deformation mode in LD and TD specimens for both materials. First-order pyramidal slip of $<a>$ dislocations is the second most frequent mode of deformation. The first order pyramidal $<c+a>$ slip systems were mostly active in TD-specimens. No evidence of pyramidal $<c+a>$ slip family of the second order was found. Twinning was shown to become operative only at later stages of deformation (at $\varepsilon_p \geq 8\%$), at a lower content of oxygen (for Grade 2). An increase in oxygen content promotes prismatic and pyramidal $<c+a>$ glide and suppresses basal slip and twinning according to Barkia (2014).

2.2. Experimental evidence of strain aging

The engineering stress-strain curves of CP Ti of Grade 2 and Grade 4 strained at 2×10^{-4} s^{-1} are shown in Fig. 3 (a). Both materials show a higher yield stress when specimens are tested along the TD than along the LD. Such anisotropic response can be explained by the lower Schmid factor for $<a>$ prismatic slip for tension along TD and by the higher CRSS for the more favorably oriented $<c+a>$ pyramidal glide in the TD direction. For that orientation the activation of $<c+a>$ pyramidal slip, with the highest CRSS, has been repeatedly observed experimentally, see Pujol et al. (1995), Barkia et al. (2015a), just after the yield drop and is expected to contribute to the higher flow stress recorded along the TD. The measured yield stress and elastic modulus are given in Table 2. The anisotropic mechanical response of the material in LD and TD directions is mainly due to the pronounced texture, which is a consequence of the rolling processing (Nixon et al., 2010). A stress peak followed by a slight yield drop and a stress plateau are observed in Fig. 3 for both Grade 2 and Grade 4 at small strains for the specimens loaded along TD. The stress drop slightly increases with the oxygen level (i.e. for Grade 4). The stress peak and plateau were not

Table 1
Chemical composition of the titanium used in this study (wt. ppm).

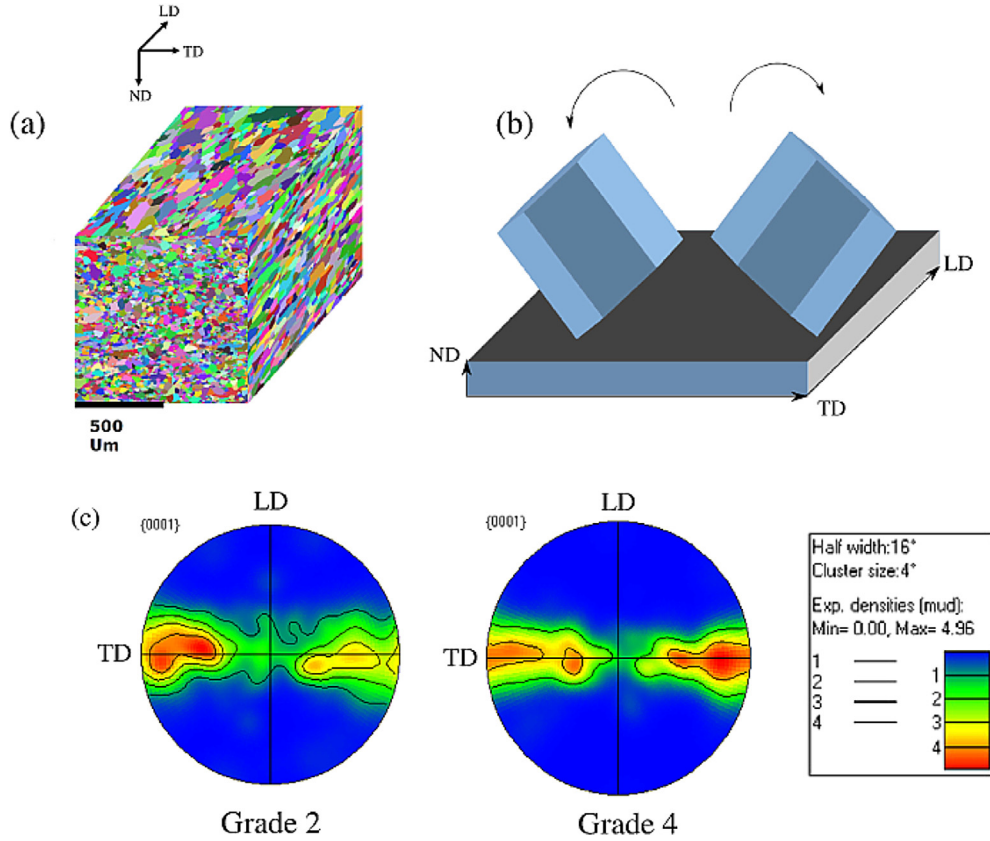|	H	O	C	Fe	N
Grade 2	6 ± 2	1600 ± 50	40	340	30
Grade 4	15 ± 3	3200 ± 100	70	1700	60

Fig. 2. (a) Initial 3D microstructure for Grade 2. (b) Schematic illustration of crystal orientation withing the sample. (c) (0001) pole figure of Grade 2 and Grade 4, after Barkia (2014).

observed in tension along LD for either Grade 2 or Grade 4. The present study will concentrate on the identification of the behavior of Grade 4.

Fig. 3 (b) illustrates a tensile test conducted at $\dot{\varepsilon} = 2 \times 10^{-3} \text{ s}^{-1}$ on a flat tensile specimen of Grade 4 in TD with complete unloading and reloading without hold time. The systematic reappearance of the yield peak after each reloading suggests a phenomenon of SSA, even though the material was not aged before reloading. The absence of the first peak on the stress-strain curve can be attributed to likely slight misalignment of the specimen/tensile grips assembly for this specific experiment.

The strain rate sensitivity (SRS) of the material was determined in the tensile tests with strain rate jumps ranging from 2×10^{-2} to $2 \times 10^{-6} \text{ s}^{-1}$. The SRS parameter is defined as:

$$SRS = \left(\frac{\partial \sigma}{\partial \log \dot{\varepsilon}_p} \right)_{T, \varepsilon_p} \tag{1}$$

where σ is the tensile stress and $\dot{\varepsilon}_p$ is the axial plastic strain rate. Small serrations in both TD and LD samples typical for the PLC effect are observed on the stress-strain curves corresponding to strain rates of 2×10^{-5} and $2 \times 10^{-6} \text{ s}^{-1}$. The amplitude of these serrations increase from 1 to 6 MPa as the strain-rate decreases from 2×10^{-4} to $2 \times 10^{-6} \text{ s}^{-1}$ in Fig. 4. The amplitude of the detected serrations largely exceeds the noise of the load cell (0.22 MPa), and cannot be ascribed to the tensile testing machine. The apparent macroscopic SRS during the jump tests between $2 \times 10^{-5} \text{ s}^{-1}$ and $2 \times 10^{-6} \text{ s}^{-1}$ remains positive. Note that additional tensile tests at lower strain rates should be carried out in order to explore possible negative values of the SRS parameter. A physical interpretation of the existence of serrations or PLC effect in the presence of positive apparent SRS will be proposed and discussed in the next section.

3. Proposed scenario for the anomalous behavior of CP α-Ti

Based on the literature results presented in the introduction, a physical interpretation of the origin of the anomalous yield point and serrations on the stress-strain curves in terms of the main deformation mechanisms in CP α-Ti at room temperature is proposed in the present section.
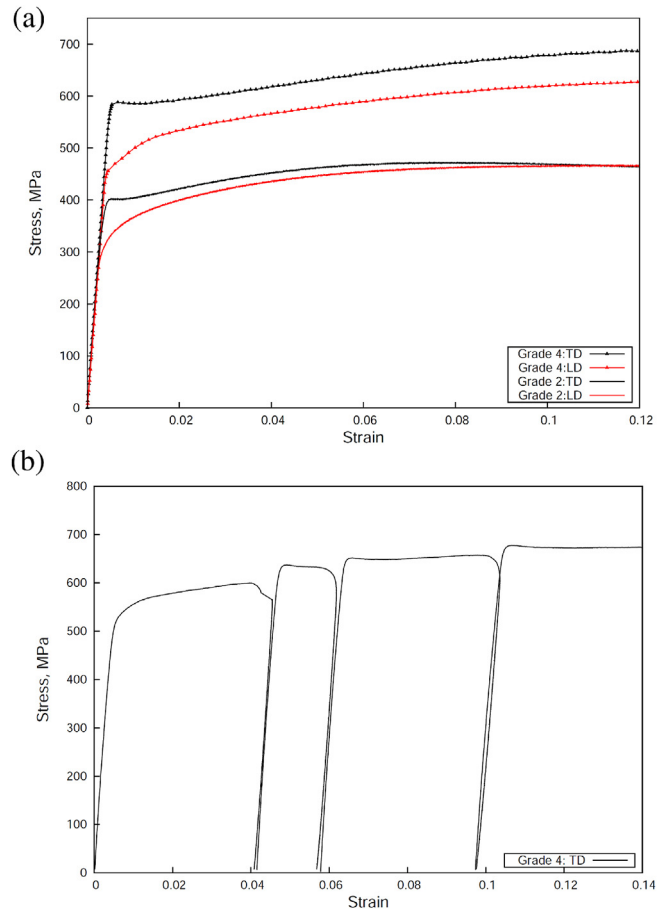
(a)

(b)

Fig. 3. Tensile tests on Grade 4: (a) on the cylindrical specimen in TD and LD at $\dot{\varepsilon} = 2 \times 10^{-4}$ s^{-1}, after Barkia (2014), (b) on the flat tensile specimen in TD with unloading and reloading without hold time, $\dot{\varepsilon} = 2 \times 10^{-3}$ s^{-1} (this work).

Table 2
Young's modulus (E) and yield stress (σ_{ys} at 0.2% strain) for Grade 2 and Grade 4.

Grade	Orientation	E (GPa)	σ_{ys} (MPa)
Grade 2	LD	114	330
	TD	118	404
Grade 4	LD	112	473
	TD	121	592

The presence of a yield stress peak followed by a plateau on the tensile curves of TD-samples can be explained by two strengthening mechanisms simultaneously active in the material: dislocation pinning by solute drag forces exerted on moving dislocations (static strain aging or time hardening) and forest type mechanism resulting from the multiplication of dislocations on several interacting slip systems (strain hardening). When age hardening is locally absent or vanishes, strain hardening at high local strain rate takes over and raises the local flow stress of the material to a level similar to that of the aged material (Strudel, 1984; Graff et al., 2004).

Hardening by solute atom segregation is based on the elastic interaction between dislocations and solute atoms that can take two forms: (1) Snoek ordering of interstitial solute atom pairs in the stress field of dislocations and (2) Cottrell clouds produced by bulk diffusion of solute atoms around edge dislocations. Following the Schoeck and Seeger (1959) interpretation of the Snoek-effect (Snoek, 1941), an ordering (short-distance rearrangement) of solute interstitials can take place in the immediate vicinity of the dislocation core where the strain distortion of the line is optimal. Snoek pinning of dislocations by paired defects has been invoked as the applicable mechanism in α-Zirconium by Paula et al. (1971), Kelly and Smith (1973). In the investigation of the effects of irradiation on Zircaloy-2 (Veevers and Rotsey, 1968; Veevers and Snowden, 1973) oxygen–oxygen pairs were found to be responsible for strain aging. Later in the work of Lacombe (1985a) it was also concluded that the rapid strain aging in Ti is mainly due to the Snoek ordering of interstitial atoms of oxygen in the stress field of
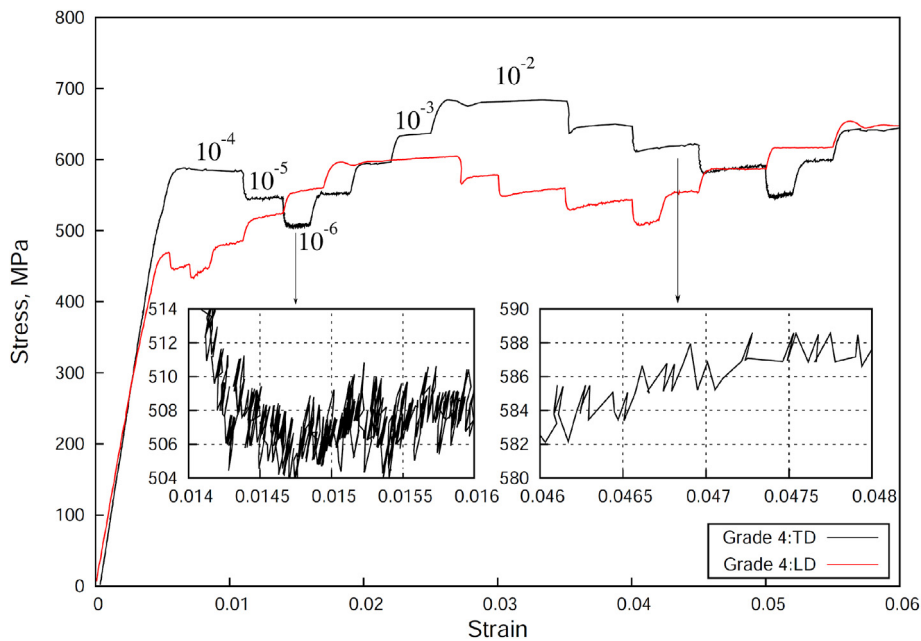
Fig. 4. Jump tests on the cylindrical specimens on Grade 4 in TD and LD at $\dot{\varepsilon} = 2 \times 10^{-2} - 2 \times 10^{-6}$ s^{-1}, after Barkia (2014).

dislocations. During aging, interstitial atoms in the close neighborhood of the dislocation core rearrange by jumps of small amplitude to occupy octahedral sites, thereby minimizing the elastic distortion of the lattice induced by these foreign atoms and the free energy of their interaction with the dislocations. An increment in the flow stress is then required to free dislocations from the free energy valleys thus created, according to Evans and Douthwaite (1973). Donoso and Reed-Hill (1977) argued that anelastic effects produced by oxygen ordering and dislocation pinning are not necessarily related. They suggested that the initial rise in flow stress in Ti is controlled by the drift of oxygen atoms to dislocations in agreement with Cottrell's mechanism. No matter which detailed mechanism is taking place in the present study, the phenomenon of SSA observed for the material strained along TD can possibly be interpreted by the interaction of oxygen atoms with <c+a> dislocations, mobilized in tensile specimens tested along TD.

As observed in the tensile experiments with unloading and reloading in Fig. 3 (b), the material strain hardening scheme can be divided into two contributions sketched in Fig. 5: an isotropic hardening component $r(\varepsilon) = r_0 + h(\varepsilon)$, which is dominant at room temperature and a kinematic hardening component $\boldsymbol{X}(\varepsilon)$ of lesser importance that leads to the formation of the narrow loops visible in Fig. 3 (b) due to slight backward plastic straining during unloading. This effect was already reported by Brandes and Mills (2004) who calls it 'dislocation recovery' and relates it to the reversibility of dislocation pile-ups. It becomes dominant at higher temperatures in Ti alloys (Jousset, 2008). The actual loading path of unload-reload experiments, visualized in Fig. 5, is AOA', where the main part of the tensile specimen is aging during the purely elastic unload-reload phase until the applied stress reaches $\sigma(\varepsilon) = X(\varepsilon) + r(\varepsilon) + r_{a_0}$ where r_{a_0} is the age hardening stress increment, acquired during the unload-reload stage, which gives rise to the stress peak on reloading.

The appearance of serrations on the tensile curves in both TD and LD samples at 2×10^{-6} s^{-1} is another manifestation of the presence of the age hardening phenomenon in the form of dynamic mechanisms, generally referred to as DSA. This unstable plastic flow can be attributed to the non-planar core of long and rectilinear <a> screw-type dislocations the mobility of which governs the room-temperature deformation of α-Ti (Naka et al., 1988; Farenc et al., 1993). Such a non-planar core is the source of a high-lattice friction when screw dislocations are lying in Peierls valleys and their motion can be described as series of jumps between adjacent valleys. Different mechanisms can be suggested to explain the behavior of these dislocations subjected to Peierls friction forces: (1) nucleation and propagation of the kink-pairs when dislocation jumps between adjacent Peierls valleys (Seeger, 1956); (2) Friedel-Escaig or Peierls mechanism when dislocations dissociate out of their glide plane via cross-slip (Escaig, 1968; Friedel, 1964); (3) Locking-unlocking model based on the transformation of the dislocation core between non-planar stable and metastable planar glissile configurations (Caillard and Couret, 2002; Caillard and Martin, 2003).

The observation of jerky flow in α-Ti at positive macroscopic values of SRS is rather unexpected. However, it should be noted that, at the micrometer scale, within grains, localized age hardening events followed by local strain bursts are necessarily associated with a negative SRS regime. When the amplitude of these erratic events is of minor importance, i.e., when the volume fraction of the specimen concerned at any time remains low, as it is the case at room temperature in α-Ti, serrations of small amplitude remain compatible with a macroscopic positive SRS response of the entire specimen. This feature will be proved by means of numerical simulations in the present work.
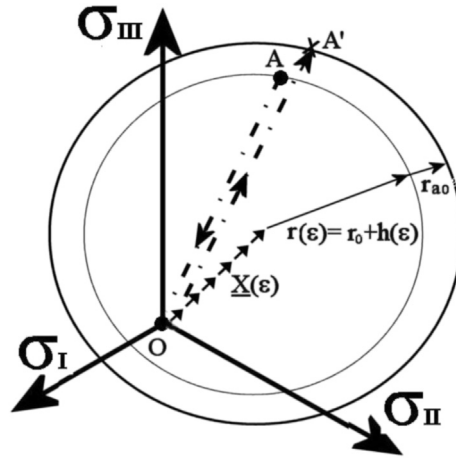
Fig. 5. Sketch of the strain hardening components at work: $X(\varepsilon)$ is kinematic hardening, $r(\varepsilon)$ is isotropic hardening and $\mathbf{r}_{a_0}$ is age hardening (see Eq. (11)). The axes $\sigma_I, \sigma_{II}, \sigma_{III}$ denote the principal deviatoric stress values.

Additional confirmation of the proposed scenario can be found in the TEM observations of the dislocation microstructure carried out by H. Jousset (Jousset, 2008) on Ti-6242. At room-temperature, pyramidal <c+a> dislocations tend to have an edge character (Fig. 6 (a)). The movement of these long edge dislocations is governed by the movement of small screw segments by a macro kink-pair mechanism. As can be seen in the scheme 1 of Fig. 6 (a), under an applied shear stress, edge segments start moving, creating multiple screw segments on the dislocation, called super-kinks. It was concluded that SSA is due to the pinning of the pyramidal <c+a> edge dislocations by the solute atoms of oxygen.

Dislocations of <a>-type slip systems tend to have a screw character (Fig. 6 (b)) and DSA can be attributed to the non-planar core of these dislocations. The local occurrence of cross-slip (scheme 2) was observed when prismatic screw <a>-type dislocations cross slip temporarily onto the basal plane, thus generating numerous screw dipoles and dislocation debris (D in Fig. 6 (b)) and also leading to wavy slip lines. More precisely, a prismatic <a> type screw dislocation which is
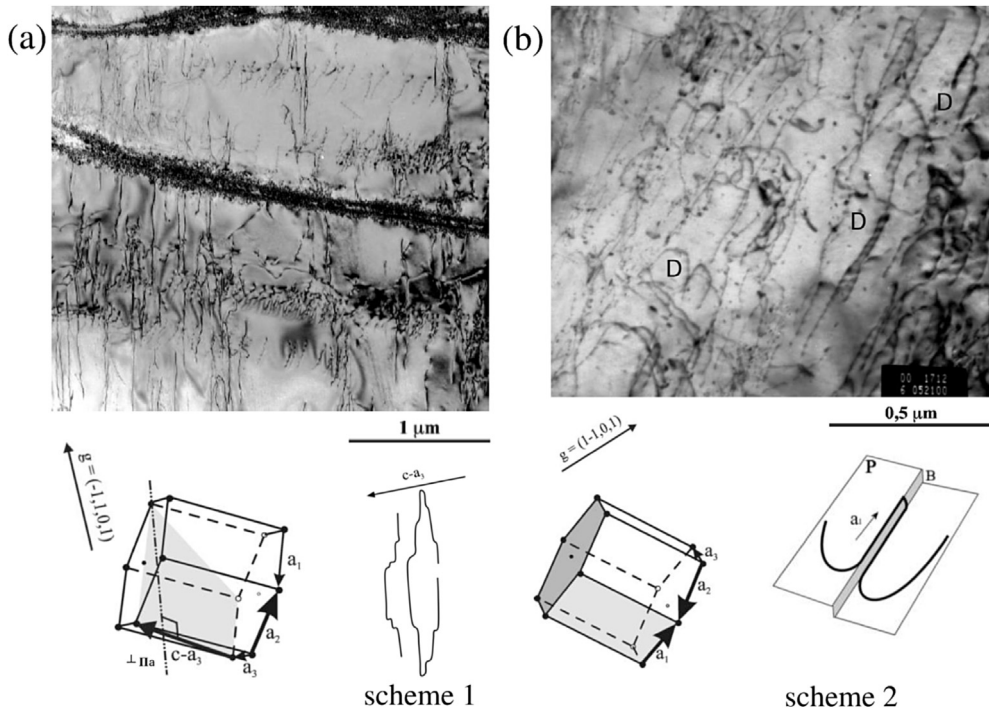

Fig. 6. TEM observations of Ti-6242 after creep: (a) at 840 MPa at $\varepsilon_p = 3.4\%$ at 20 °C. (b) at 780 MPa at $\varepsilon_p = 8\%$ at 150 °C (taken from the work by Jousset (2008)).

in a stable sessile and immobilized configuration (pinned state) is shown to cross-slip onto the basal plane, thus changing its configuration to mobile metastable glissile causing dislocation jump (unpinned state). As described in the literature (Couret and Caillard, 1991; Caillard and Martin, 2003), the sessile core structure of immobile screw dislocations can recombine into planar, glissile and metastable configurations in one of the three possible glide planes. Thus, pinned by their core structure, screw dislocations in this waiting position can be mobilized by the arrival of individual or even more efficiently by groups of dislocations that will form dislocation avalanches and generate localized strain bursts (Jousset, 2008).

The presence of localized strain bursts, recorded at room temperature in tension as well as in relaxation tests in Ti alloys (Jousset, 2008) and in Ti—O pillars deformed *in-situ* by TEM (Yu et al., 2015) implies local values of strain and strain rates in drastic excess of the macroscopic strain and strain rate experimentally imposed to the test piece. Depending on the amplitude of these self-organized critical dynamic (SOCD) events (Fressengeas et al., 2005; Bharathi et al., 2002), smaller or larger elastic unloading of the testing machine can occur and are recorded as 'serrations' of various amplitude, testifying the negative sign of the local SRS. On the other hand, even in the absence of detectable serrations involving unloading, plasticity in crystalline materials has been recognized as intermittent or chaotic in time, a phenomenon enhanced in materials exhibiting PLC effects (Weiss et al., 2007; Lebedkina and Lebyodkin, 2008). In the absence of plastic activity during these 'waiting periods', aging of the material is taking place even though the macroscopic strain rate is kept constant. Hence, we can conclude that, locally, the aging of the material and the pinning of dislocations cannot be directly controlled by the testing equipment. The state of aging of a tensile sample remains as a specific response of the crystal, the grain or an array of grains to the particular stress, strain, temperature and strain rate distribution they are exposed to.

At room temperature, Ti and its alloys when tested at macroscopic 'constant strain rates' in the range 10^{-3}—10^{-9} s^{-1} will exhibit positive macroscopic SRS values since these testing conditions encompass the low temperature/high strain rate boundary of the PLC domain; yet for the lower strain rate values, prolonged aging periods will favor the formation of SOCD phenomena or small strain bursts responsible for the A-type serrations observed on the stress-strain curves. They are generally preceded by a sudden increase in flow stress above the base line of the stress-strain curve due to localized age hardening events.

The previous mechanisms of SSA and DSA were implemented in the present study in the formulation of a phenomenological strain aging model written at the grain scale and described in the next section.

4. Constitutive model

The original formulation of the phenomenological viscoplastic model of strain aging proposed by Kubin and Estrin (1985); McCormick (1988), labeled KEMC, is based on an implicit mathematical description of an homogeneous material exhibiting a negative SRS behavior without reference to any space or time scale. In order to describe the various observations reported above, several different length scales must be introduced in a more elaborate model.

The self organization of plasticity events in the crystalline metallic material rests on the ability, for basic physical objects or entities, to interact on different scales: (*i*) dislocation lines, their intimate structure in the distorted crystal and their interactions with solute impurity atoms. For the sake of simplicity the present model is synthesizing these time-dependent phenomena under the general term of 'age hardening phenomena' (Graff et al., 2004), with a characteristic time t_a, introduced in the equation describing the local level of the flow stress. (*ii*) the movement and the multiplication of dislocations is described by a shear strain along the various glide planes and in the directions of the respective Burgers vectors. The mutual interaction of dislocations is globally characterized by the strain hardening component of the flow stress at all Gauss points of each crystalline grain in the finite element mesh. (*iii*) the introduction of a texture (statistically representative or EBSD realistic) into the polycrystalline model that can also handle the cooperative interactions between neighboring grains toward general plasticity (Barbe et al., 2001b), as well as the local inhibition of it, in case of less favorable arrangements of grain orientations, or age hardening events.

Thus, by combining the KEMC approach and a finite element (FE) polycrystalline model, it becomes possible to obtain an accurate description of the local stress and strain field distributions as well as a map of the strain rate heterogeneities that develop during mechanical testing in a textured, polycrystalline α-Ti assembly (Quey et al., 2011). Depending on the set of chosen parameters the model can be used for both static and dynamic strain aging simulations (Colas et al., 2014).

4.1. Age hardening single crystal model

The continuum crystal plasticity model used in the present study is based on the age hardening constitutive model proposed by Zhang et al. (2001). An additional internal variable t_a called aging time was introduced by these authors in the isotropic theory of von Mises plasticity. The originality of the present work lies in the fact that such aging time variables are incorporated into a crystal plasticity model for the simulation of time hardening phenomena for full-field simulations of polycrystalline aggregates.

Four slip systems families were considered in the present model: three of them with <a>-type Burgers vector and the fourth one with <c+a>-type Burgers vectors (see Table 3).

Table 3
Slip systems families of α-Ti considered in this work.

Slip family $F(s)$	Plane and direction	Slip systems s	ϕ
1. Basal $<a>$	$\{0001\}<1\bar{2}10>$	1, 2, 3	I
2. Prismatic $<a>$	$\{10\bar{1}0\}<1\bar{2}10>$	4, 5, 6	II
3. Pyramidal $<a>$	$\{10\bar{1}1\}<1\bar{2}10>$	7, 8 … 12	III
4. Pyramidal $<c+a>$	$\{10\bar{1}1\}<11\bar{2}3>$	13, 14 … 24	IV

The full list of slip systems is given in Table 4. In total, 24 slip systems are accounted for, $N_{total} = \sum_{F=1}^{4} N_F = 24$. We introduce the function $F(s)$ which gives the label of the family which the slip system s belongs to. Each of the four slip systems families represents a set ϕ of the corresponding slip systems s. The attribution of the slip system numbers to the set $\phi_{F(s)}$ is as follows:

If $1 \leq s \leq 3$, then $F(s) = I$ and the corresponding set $\phi_I = \{1,2,3\}$.

If $4 \leq s \leq 6$, then $F(s) = II$ and the corresponding set $\phi_{II} = \{4,5,6\}$.

If $7 \leq s \leq 12$, then $F(s) = III$ and the corresponding set $\phi_{III} = \{7,8,9,10,11,12\}$.

If $13 \leq s \leq 24$, then $F(s) = IV$ and the corresponding set $\phi_{IV} = \{13,14,\ldots,24\}$.

The resolved shear stress τ^s on each slip system s is defined as:

$$\tau^s = \underset{\sim}{\sigma} : \underline{m}^s = \underset{\sim}{\sigma} : \frac{1}{2}\left(\underline{l}^s \otimes \underline{n}^s + \underline{n}^s \otimes \underline{l}^s\right) \tag{2}$$

where $\underline{l}^s$ and $\underline{n}^s$ are unit vectors directed along the slip direction and normal to the slip plane, respectively. The stress tensor is $\underset{\sim}{\sigma}$. The plastic strain rate is the sum of the slip rates on all slip systems N_{total}:

$$\underset{\sim}{\dot{\varepsilon}}^p = \sum_{s=1}^{N_{total}} \dot{\gamma}^s \underline{m}^s \tag{3}$$

According to Schmid's law, the yield function f^s is defined as:

$$f^s(\tau^s, r^s) = |\tau^s| - r^s \tag{4}$$

Each slip system family possesses its own material parameters labeled with the exponent $F(s)$. The plastic strain rate $\dot{\gamma}^s$ on each slip system s is determined by a hyperbolic viscoplastic flow rule:

Table 4
The full list of slip systems of α-Ti considered in this work.

System number	Slip plane	Slip direction	Slip system family $F(s)$
Basal $<a>$ $(0001)<1\bar{2}10>$			
1	(0001)	$[1\bar{2}1\,0]$	I
2	(0001)	$[2\bar{1}\bar{1}\,0]$	I
3	(0001)	$[11\bar{2}\,0]$	I
Prismatic $<a>$ $\{10\bar{1}\,0\}<1\bar{2}10>$			
4	$(10\bar{1}\,0)$	$[1\bar{2}\,10]$	II
5	$(01\bar{1}\,0)$	$[2\bar{1}\bar{1}\,0]$	II
6	$(\bar{1}100)$	$[11\bar{2}\,0]$	II
Pyramidal $\pi_1 <a>$ $\{10\bar{1}\,1\}<11\bar{2}0>$			
7	$(10\bar{1}\,1)$	$[1\bar{2}\,10]$	III
8	$(01\bar{1}\,1)$	$[2\bar{1}\bar{1}\,0]$	III
9	$(\bar{1}101)$	$[11\bar{2}\,0]$	III
10	$(\bar{1}011)$	$[1\bar{2}\,10]$	III
11	$(0\bar{1}\,11)$	$[2\bar{1}\bar{1}\,0]$	III
12	$(1\bar{1}\,01)$	$[11\bar{2}\,0]$	III
Pyramidal $\pi_1 <a+c>$ $\{10\bar{1}\,1\}<11\bar{2}3>$			
13	$(10\bar{1}\,1)$	$[2\bar{1}\bar{1}\,3]$	IV
14	$(10\bar{1}\,1)$	$[11\bar{2}\,3]$	IV
15	$(01\bar{1}\,1)$	$[11\bar{2}\,3]$	IV
16	$(01\bar{1}\,1)$	$[\bar{1}2\bar{1}\,3]$	IV
17	$(\bar{1}101)$	$[\bar{1}2\bar{1}\,3]$	IV
18	$(\bar{1}101)$	$[\bar{2}\,113]$	IV
19	$(\bar{1}011)$	$[\bar{2}\,113]$	IV
20	$(\bar{1}011)$	$[\bar{1}\bar{1}\,23]$	IV
21	$(0\bar{1}\,11)$	$[\bar{1}\bar{1}\,23]$	IV
22	$(0\bar{1}\,11)$	$[1\bar{2}\,13]$	IV
23	$(1\bar{1}\,01)$	$[1\bar{2}\,13]$	IV
24	$(1\bar{1}\,01)$	$[2\bar{1}\bar{1}\,3]$	IV

$$\dot{\gamma}^s = \dot{v}^s sign(\tau^s), \quad \dot{v}^s = \dot{v}_0^{F(s)} \sinh\left\langle \frac{f^s}{\sigma_0^{F(s)}} \right\rangle \tag{5}$$

The hardening law in the model consists of a non-linear isotropic hardening function including the interaction matrix h_{rs} between the slip systems, in addition to the initial critical resolved shear stress (CRSS), $\tau_0^{F(s)}$,

$$r^s = \tau_0^{F(s)} + Q^{F(s)} \sum_{r=1}^{24} h_{rs} \left[1 - \exp\left(-b^{F(r)} v^r \right) \right] \tag{6}$$

Kinematic hardening should be introduced for a better description of relaxation effects but it is not done here for the sake of simplicity (Siska et al., 2007). The interaction matrix includes self (diagonal coefficients of the submatrices: h_1^b, h_1^p, $h_1^{\pi_1}$...) and latent (off-diagonal components of the matrix: h_p^b, $h_{\pi_1}^b$, $h_{\pi_1}^p$...) hardening coefficient following (Parisot et al., 2000). This also includes interaction hardening between slip systems belonging to distinct families. The interaction matrix $[Q^{F(s)}h_{rs}]$ is given by Eq. (7). Very little information is available regarding the values of the matrix coefficients h_{rs} for HCP metals including α-Ti. Hence, due to the lack of the relevant data, the isotropic interaction is adopted with $h_{1,2}^{F(s)} = 1$ and $h_{F(r)}^{F(s)} = 1$, $s \neq r$ for all matrix coefficients.

$$[Q^{F(s)}h_{rs}] = \begin{array}{c} \\ basal \\ prism \\ \pi_1 \\ \vdots \end{array} \begin{pmatrix} \overset{basal}{Q^b \begin{pmatrix} h_1^b & h_2^b & \cdots \\ h_2^b & h_1^b & \cdots \\ h_2^b & h_2^b & \ddots \end{pmatrix}} & \overset{prism}{Q^b h_p^b} & \overset{\pi_1}{Q^b h_{\pi_1}^b} & \overset{\cdots}{} \\ & & & \cdots \\ Q^p h_b^p & Q^p \begin{pmatrix} h_1^p & h_2^p & \cdots \\ h_2^p & h_1^p & \cdots \\ h_2^p & h_2^p & \ddots \end{pmatrix} & Q^p h_{\pi_1}^p & \cdots \\ Q^{\pi_1} h_b^{\pi_1} & Q^{\pi_1} h_p^{\pi_1} & Q^{\pi_1} \begin{pmatrix} h_1^{\pi_1} & h_2^{\pi_1} & \cdots \\ h_2^{\pi_1} & h_1^{\pi_1} & \cdots \\ h_2^{\pi_1} & h_2^{\pi_1} & \ddots \end{pmatrix} & \cdots \\ \vdots & \vdots & \vdots & \ddots \end{pmatrix} \tag{7}$$

A more sophisticated description of single crystal hardening could be used involving dislocation densities as internal variables, as proposed by Alankar et al. (2011) for α-titanium. Such physically-based constitutive equations have proved to be very effective in recent years. A simpler approach is used in the present work because first values of the material parameters were already identified for the same material by Doquet and Barkia (2015) in the absence of age hardening effect. One of the main guidelines of this paper, which was ignored in previous articles, is to introduce the age hardening (time-dependent) component of the flow stress of this class of materials, in relation with the appropriately active slip systems, within a textured crystalline aggregate.

An aging time variable, $t_a^{F(s)}$, is introduced for each slip system family. The aging time increment is computed from an evolution law depending on the viscoplastic strain rate, $\dot{\vartheta}^{F(s)}$, of the corresponding family:

$$\dot{t}_a^{F(s)} = 1 - \frac{t_a^{F(s)} \dot{\vartheta}^{F(s)}}{\omega^{F(s)}} \tag{8}$$

with the initial condition $t_a^{F(s)}(t = 0) = t_{a_0}^{F(s)}$, where $t_{a_0}^{F(s)}$ determines the initial pinning of dislocations leading to the anomalous yield point. The accumulated strain rate $\dot{\vartheta}^k$ for the slip system family $k = I,II,III$ or IV, is the sum of the cumulative slip rates on the slip system s in the set ϕ_k:

$$\dot{\vartheta}^k = \sum_{r \in \phi_k} \dot{v}^r \tag{9}$$

Aging phenomena are characterized by an additional time hardening component of the flow stress. The corresponding hardening term, $r_a^{F(s)}$, depends on the new internal variable $t_a^{F(s)}$ in the form:

$$r_a^{F(s)} = r_{a0}^{F(s)} \left[1 - \exp\left(-\left(\frac{t_a^{F(s)}}{t_0^{F(s)}} \right)^{\beta^{F(s)}} \right) \right] \tag{10}$$

where $t_a^{F(s)}$ is a time dependent function and $t_0^{F(s)}$ is the characteristic time of the aging process (diffusion of impurity atoms or core splitting). The β parameter controls the span of the SRS domain (Mazière et al., 2010). The parameter t_{a0} depends on prior

aging history of the material. The yield function f^s given by Eq. (4) is amended, so as to include the additional hardening term r_a:

$$f^s(\tau^s, r^s) = \left|\tau^s\right| - r^s - r_a^{F(s)} \tag{11}$$

According to the generalization of Schmid's law, viscoplasticity occurs when f^s becomes positive. The model was implemented in the finite element code *Z-Set* (Zset Software, 1996). The resolution method is based on an implicit Newton–Raphson algorithm. The numerical integration of constitutive equations is performed at each Gauss point of each element using a second-order Runge-Kutta method with automatic time stepping (Besson et al., 2010).

4.2. Polycrystalline aggregates

In real polycrystals the averaged response of the grains is strongly dependent on the crystallographic orientation and on the constraints due to neighboring grains (Barbe et al., 2001b). The objective of the present work is to study the deformation modes induced by strain aging in the grains of a polycrystal. This is why several 2D and 3D polycrystalline aggregates were generated via Voronoï tessellation following Osipov et al. (2008); Cailletaud et al. (2003). This model reproduces grains with a given crystallographic orientation and mechanical constitutive equations, allowing to account for the heterogeneity of polycrystalline structures (Barbe et al., 2001a). 2D simulations make it easy to observe localization phenomena inside grains and their possible transmission through grain boundaries. Several realizations for statistical representativity of 2D samples were carried out. Validation of the observations is performed on 3D grain samples with periodic boundary conditions. Fig. 7 (a,b) presents two flat polycrystalline arrangements with dimensional ratio of $\frac{L}{W} = 2.5$, where L and W are the length and the width of the sample, respectively. The aggregates consist of 71 and 432 grains, respectively. The average FEM mesh size is $\simeq W/25$. Note that '2D' means that an extruded mesh was used with columnar grains with a single element, a
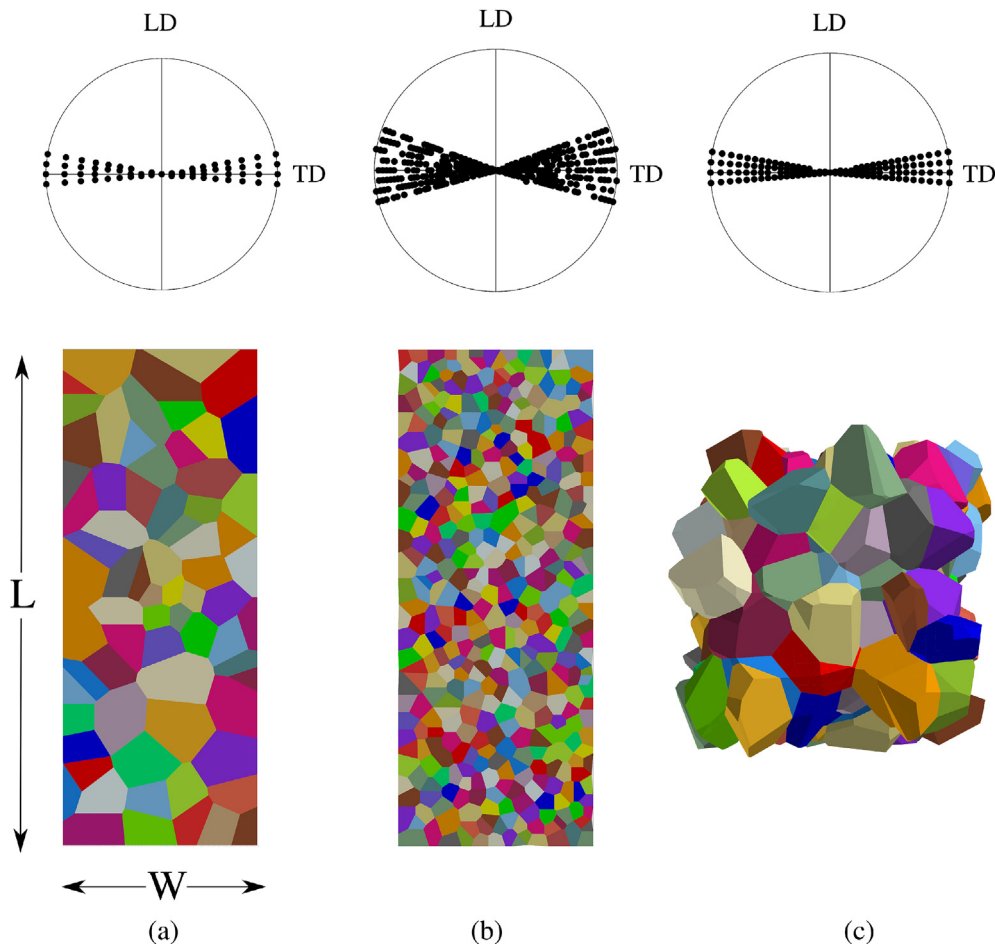

Fig. 7. Crystallographic texture used in the simulation and spatial distribution of: (a) 71 2D grains; (b) 432 2D grains; (c) 150 3D grains.

20-node quadratic brick element with reduced integration, in the thickness. One element within the thickness and free outer surfaces are used so that the conditions are close to plane stress conditions. The results would depend on the plate thickness but then several elements within the thickness should be used in order to avoid elongated elements not suitable for FE simulations. As a first step, an idealized texture was used due to the limited number of grains. The crystallographic orientations corresponding to the texture presented on the pole figures of Fig. 7 were ascribed to the grains. Fig. 7 (c) shows the obtained geometry of a 3D aggregate of 150 grains made with 100 × 100 × 100 µm mesh with 15-node quadratic 3D tetrahedral continuum elements (eighteen Gauss points per element) with periodic boundaries.

The role of grain boundaries in the present model is handled by the usual FEM approach which simply warrants continuity of displacement and of stress vector between neighboring grains. More detailed and accurate descriptions of the contribution of grain boundaries to the overall plasticity of the polycrystalline aggregate have been proposed in the literature either based on phenomenological description of the interactions between slip systems of neighboring grains for intergranular sliding and cracking by Musienko and Cailletaud (2009) or involving higher order continuity requirements in strain gradient plasticity Cordero et al. (2012) and a detailed description of the physical structure of the grain boundaries by Taupin et al. (2013). In the present study, the contribution of grain boundary sliding and other detailed interaction mechanisms to the plastic behavior of α-titanium at room temperature and within the range of strain rates explored, can be ignored. At higher temperatures and under creep conditions, this assumption would no longer hold and an appropriate description of the contribution of grain boundaries to plasticity should be introduced in the model.

Ultimate comparison with experimental observations at free surfaces requires precise account of the 3D geometry of grains emerging at the surface, as demonstrated by systematic FE simulations of the free surface effect by Zeghadi et al. (2007) and Zhao et al. (2008).

5. Identification of materials parameters

5.1. Identification strategy

A rapid estimate of the elastic-viscoplastic material parameters was first performed with the help of a homogenized polycrystal model (Cailletaud, 1992; Berveiller and Zaoui, 1978) in which the mechanical fields are homogeneous per grain orientation, so that the specimen can be considered as a volume element. At this step, the aging contribution of the material parameters was disregarded. Next step was the identification of the aging parameters and validation of the ability of the model to capture the main features of the strain localization phenomena associated with the anomalous yield point and PLC effect. For this purpose, full-field FE simulations are required on the '2D' polycrystalline aggregates of Fig. 7 (a,b). Finally, simulations on the 3D polycrystalline aggregates (like in Fig. 7 (c)) were carried out in order to obtain a more quantitative estimate of the material's response. The typical computation time (CPU time) for a precision ratio of 10^{-4} for tensile tests up to $\varepsilon = 2\%$ overall strain ranges from 7 to 10 h for 2D simulations and from 28 to 33 h for 3D simulations.

5.2. Identification procedure for viscoplastic material parameters

The identification of the viscoplastic parameters is performed on flat polycrystalline specimens with either 71 or 432 columnar grains with ascribed crystallographic orientations corresponding to the texture of the pole figures of Fig. 7 (a,b). Vertical displacements are applied at the top edge of the mesh (keeping the bottom edge fixed) thus imposing the macroscopic strain and strain rate on the sample at all times, as an infinitely hard machine would do. All lateral faces are free of forces. The identified viscoplastic material parameters are given in Table 5. In order to activate the right systems at the right time, appropriate CRSS should be prescribed. Many researchers investigated the CRSS of Ti and its alloys under various conditions of temperature and composition (Gong and Wilkinson, 2009; Zaefferer, 2003; Conrad, 1981; Li et al., 2013; Battaini, 2008), however, to date, there is no consensus on the precise values of CRSS. For the ease of the comparison, the value of CRSS for various slip systems is usually normalized by the CRSS of the easiest deformation mode. In the present study, the slip trace analysis based on the results of EBSD was employed to estimate the CRSS in CP α-Ti following Barkia (2014), Bridier et al. (2005), Li et al. (2012). Table 5 gives the list of the CRSS of slip families used in the simulations. The apparent CRSS includes the additive term of hardening due to aging, i.e. $\tau_0^{F(s)} + r_{a_0}^{F(s)}$. In a second step, $r_{a_0}^{F(s)}$ is identified. The provided values of the CRSS can be compared to the corresponding values in the model by Doquet and Barkia (2015) where age hardening is not explicitly introduced in the crystal plasticity model. The targets for identification are the macroscopic tensile

Table 5
Values of material parameters used in the aging single crystal model.

Slip systems family	$\tau_0^{F(s)}$ (MPa)	$r_{a_0}^{F(s)}$ (MPa)	$\tau_0^{F(s)} + r_{a_0}^{F(s)}$ (MPa)	$t_0^{F(s)}$ (s)	$\frac{\omega^{F(s)}}{t_0^{F(s)}}$ (s^{-1})
Basal <a>	232	30	262	10	10^{-6}
Prismatic <a>	161	30	191	10	10^{-6}
Pyramidal <a>	189	30	219	10	10^{-6}
Pyramidal <c+a>	189	110	299	100	10^{-7}

responses corresponding to the tests reported in Section 3 and the hierarchy of local slip system activation inside the grains reported in the statistical analysis of slip lines by Barkia et al. (2015a).

The elastic stiffness tensor exhibits transversely isotropic symmetry because of the crystallographic structure of α-Ti with the following single crystal elastic constants: $C_{11} = 154$ GPa, $C_{33} = 183$ GPa, $C_{44} = 46$ GPa, $C_{12} = 86$ GPa, $C_{13} = 67$ GPa from Flowers et al. (1964), Fisher and Renken (1964). The viscoplastic parameters σ_0 and $\dot{\vartheta}_0$ were identified from the tensile tests with strain rate jumps. For simplicity, these parameters are given the same value for all slip families, i.e. $\sigma_0 = 10$ MPa and $\dot{\vartheta}_0 = 1.6 \times 10^{-6}$ s^{-1}. The experimental stress-strain curves for CP Ti show a very low hardening rate, thus a quasi-linear isotropic hardening was prescribed for all slip systems ($Q = 250$ MPa, $b = 1$).

5.3. Identification of static strain aging parameters

Following the scenario discussed in Section 3 and adopted in the present study, the origin of the anomalous yield point phenomena observed for the material loaded along TD was interpreted as resulting from the combination of two mechanisms: a higher apparent yield stress due to lower Schmid factors on all potentially active slip systems (<a> and <c+a>), immediately followed by a significant strain softening provided by the unlocking of the <c+a> pyramidal slip system and leading to either a stress peak or a plateau. This interpretation is confirmed by the quantitative observations on the contributions of individual slip systems in Grade 4 Ti reported by Barkia et al. (2015a). The PLC effect observed during the tensile tests at low strain rate for both TD and LD, is assumed to be due to the non-planar core of the <a>-type screw dislocations which can switch between sessile and glissile core configurations, causing jerky dislocation motion with a series of sudden jumps between locked positions.

In order to simulate the described scenario, two sets of distinct aging parameters are considered in the model: one for all <a>-type slip systems and the second one for <c+a>-type slip systems. The parameters were calibrated so as to locate precisely the domain of negative SRS, associated with plastic strain heterogeneities. At a given temperature, this domain exists where the flow stress decreases when strain rate increases. According to our model, the kinetics of dislocation anchoring is controlled by the parameters t_0, r_{a_0}, β, ω, and by the initial aging time t_{a_0}. The identification and the role of the parameters controlling the strain localization phenomena associated with the anomalous yield point are further discussed.

- Time t_0 characterizes the relaxation kinetics between pinned and unpinned states of the dislocations. Aging time t_{a_0} is the initial value of the internal variable t_a and characterizes the initial state of pinning of dislocations leading to the anomalous yield point. In the present model, we take sufficiently large value of t_{a_0} (1000 s) compared with t_0, in order to get a suitable description of the peak stress. It is also consistent with the long and uncontrolled aging time at room temperature experienced by most test pieces.
- The plastic strain increment ω is the amount of strain associated with the activated plastic bands when mobile dislocations have to overcome their obstacles. Its value is kept constant here and equal to 10^{-4} as in Marais et al. (2012).
- The ratio ω/t_0 determines the position of the center of the SRS < 0 domain, on the strain rate axis. In Fig. 8, the flow stress (=τ, the resolved shear stress) is plotted as a function of the plastic strain rate (log$\dot{v}$); thus the evolution of the SRS of the phenomenological macroscopic model can be visualized for each slip system family: respectively for Burgers vectors <a> and <c+a>. Analytical curves are constructed using the parameters identified in Table 5. For <c+a> slip family, the SRS curve goes through negative values at $\omega/t_0 = 10^{-7}$ s^{-1}. The SRS < 0 domain for the <a>-type slip families is centered on $\omega/t_0 = 10^{-6}$ s^{-1} and responsible for the PLC effect. Keeping the SRS < 0 domain for the <c+a> family a decade below that of the <a> slip family is consistent with the association of the <c+a> slip family with meso-Lüders shear bands and the diffusion of impurity atoms to edge dislocations. It also acknowledges the role of <a> slip systems with PLC serrations in relation with the core splitting of screw dislocations, a quicker process than the diffusion of impurity atoms.
- The parameter r_{a_0} denotes the interaction force between dislocations and solute atoms, thus it controls the pinning stress. The amplitude of the yield peak is directly related to r_{a_0} value and to the orientation of the crystals with respect to the tensile direction.
- The exponent β depends on the type of diffusion and controls the kinetics of the pinning process. In the present model the $\beta = 2/3$ which corresponds to the bulk diffusion of solute atoms along dislocation lines (Friedel, 1964).

The results of the simulations on the flat polycrystalline specimen with 71 grains for tensile tests under constant strain rate on the specimens oriented along the TD and LD directions are presented in Fig. 9. The predicted overall stress-strain curves can be compared with the experimental ones. The stress peak is observed in TD specimen and is absent in LD specimen in agreement with the experiment. The yield stress along LD is somewhat overestimated. Moreover, the stress peak appears in TD after each reloading, in accordance with experimental results (curve not presented here). It means that the unloading and reloading were long enough to allow for significant aging to occur.

5.4. Identification of dynamic strain aging parameters

Simulations of PLC effects were carried out using the set of constitutive equations and corresponding parameters described in Section 4.1. The main difference in the parameters between SSA and DSA simulations are in the values of t_0, t_{a_0}
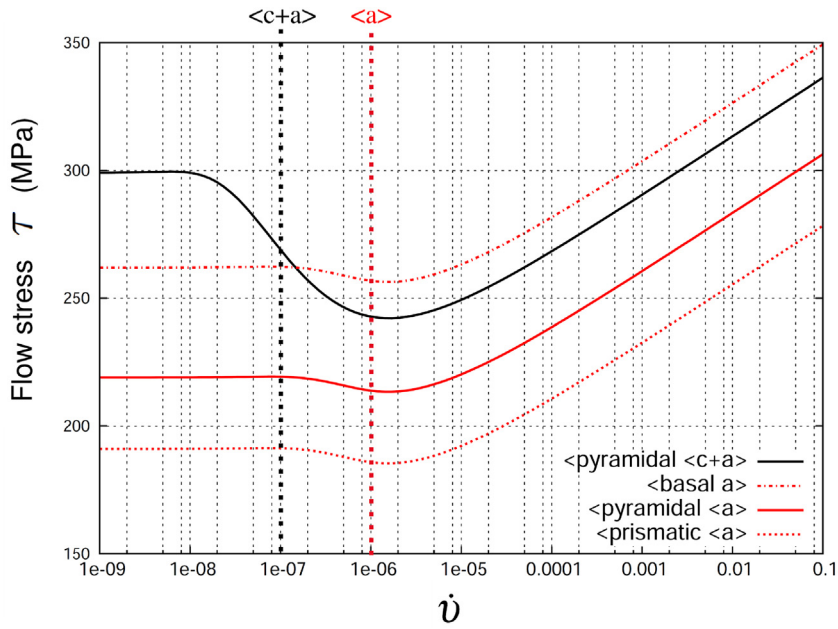
Fig. 8. The evolution of the flow stress at ($\gamma_p^s = 0$) on various slip systems as a function of strain rate according to the proposed aging single crystal model.
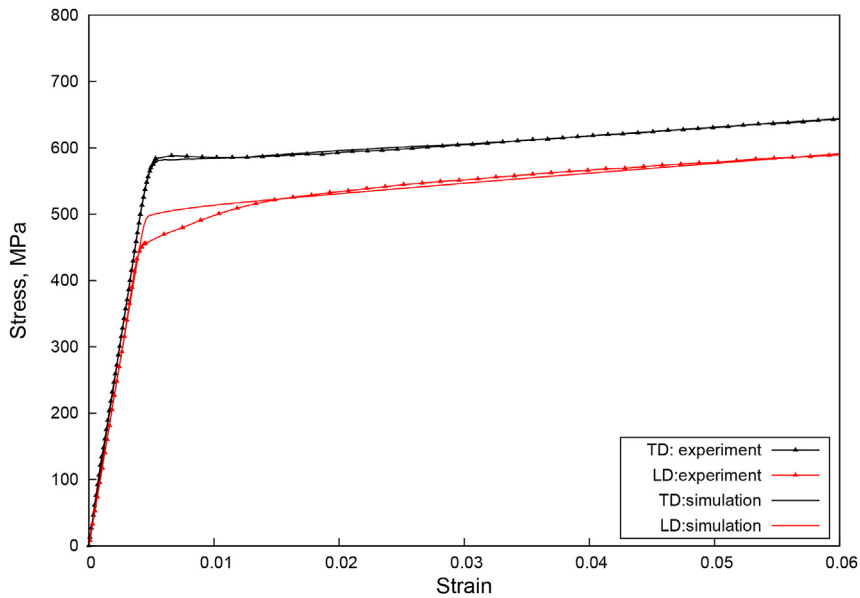

Fig. 9. Tensile test at $\dot{\varepsilon} = 2 \cdot 10^{-4} \, s^{-1}$ for Grade 4 on the 71 grain aggregate. Comparison of the model with experiment.

and r_{a_0}. As stated above, the DSA manifestation in α Ti can be ascribed to the dissociation of the $<a>$-type dislocation cores. Consequently, in the model, three slip families of $<a>$-type Burgers vector will reproduce the DSA at low strain rates.

A characteristic time t_0 for $<a>$ families, shorter than that for $<c+a>$ was chosen. It can be justified by the fact that the time necessary for the dissociation of $<a>$ dislocation cores onto various glide planes is shorter than that for the diffusion of oxygen towards the dislocations in the case of SSA. In addition, the parameter r_{a_0} corresponding to the maximal additional stress provided by the pinned state is lower for $<a>$-systems.

Using the parameters of Table 5, the simulated stress-strain curves of the tensile tests with strain rate jumps are plotted in Fig. 10. For a more legible presentation of the results, the origins of the simulated curves were slightly shifted. With the material parameters selected a correct description of the strain rate jumps and of the positive values of the strain rate sensitivity are obtained. It should be noted that at $2 \times 10^{-6} \, s^{-1}$ the PLC serrations observed on the experimental curve are
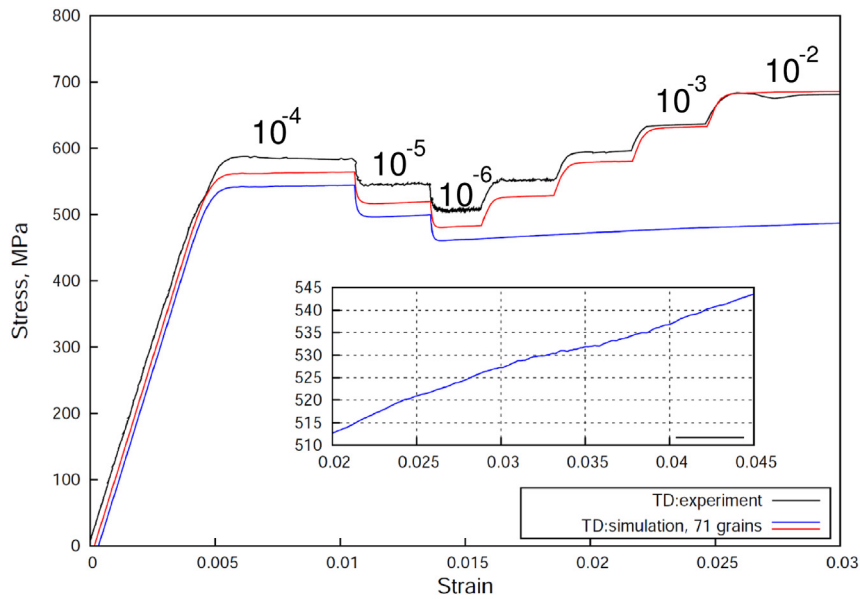
Fig. 10. Experimental and simulation curves for the 71 grain aggregate for Grade 4 of tensile test in TD with strain rate jumps. The curves are slightly shifted vertically (30–50 MPa) for clarity. The insert exhibits a vertical zoom where instabilities in flow stress are evidenced.

absent on the simulation red curve. The absence of the serrations can be explained by the short duration of the simulation at the strain rate of 2×10^{-6} s^{-1}. When carrying the tensile test simulation at 2×10^{-6} s^{-1} for a longer time (Fig. 10, blue curve), the serrated flow can be observed (see insert) on the macroscopic stress-strain curves for both TD and LD.

5.5. Prediction of PLC instabilities and plastic intermittence

The identified parameters of the strain aging model for Grade 4 (see Table 5) were used to predict the domain of NSRS associated with the PLC instabilities observed on the stress–strain curve at $\dot{\varepsilon} = 2 \times 10^{-6}$ s^{-1} (see Fig. 4). For this purpose simulations were performed on a volume element with 21 grain orientations replicating the texture presented on the pole Fig. 7. The self-consistent homogenization scheme was employed, cf. Amouzou et al., 2016.

Each simulation was carried out at a constant strain rate up to 10% strain. The range of the explored strain rates varied between 10^{-9} s^{-1} and 10 s^{-1}. Fig. 11 shows the simulated macroscopic flow stress σ as a function of the plastic strain rate $\dot{p}$, where $\dot{p} = |\dot{\varepsilon}_p|$, the axial plastic strain rate component. It can be seen that the domain of NSRS is located in the vicinity of $\dot{p} = 10^{-7}$ s^{-1} and not at 10^{-6} s^{-1} as it was predicted by the analytical curve in Fig. 8 for a single grain. It implies that the observed strain heterogeneities on the simulated stress-strain at $\dot{\varepsilon} = 2 \times 10^{-6}$ s^{-1} (see Fig. 10) were obtained in the presence of positive
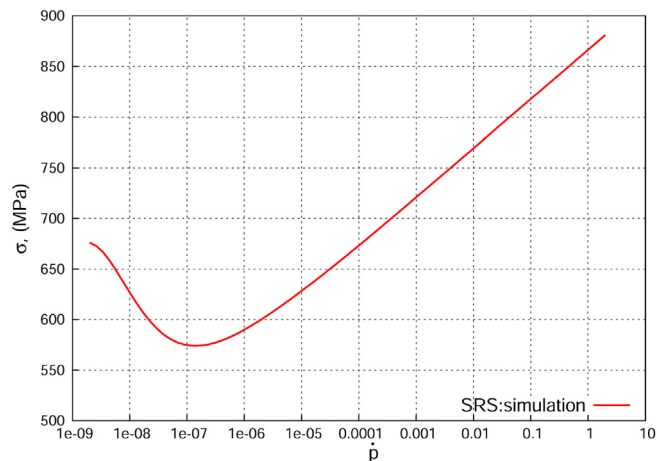

Fig. 11. Predicted evolution of strain rate sensitivity (SRS) for a polycrystalline volume element.

macroscopic SRS. Similar to the simulations, the experimentally observed serrations were also obtained in the presence of positive macroscopic SRS. In order to find the explanation to such a phenomenon, the statistical analysis of the distribution of strain rates within the grains in the simulations at $\dot{\varepsilon} = 2 \times 10^{-6}$ s^{-1} for a TD oriented specimen with 71 grains was carried out. The results are presented in the form of the histogram of Fig. 12. It can be seen that the majority of the prismatic <a> plastic flow takes place at $\dot{\varepsilon} = 10^{-6}$ s^{-1}. The same is applied to the pyramidal <c+a> dislocations. However, the second most common strain rate for prismatic <a> dislocations is $\dot{\varepsilon} = 10^{-7}$ s^{-1}, and it is $\dot{\varepsilon} = 10^{-8}$ s^{-1} for <c+a> dislocations. The present statistics shows that during the simulation at $\dot{\varepsilon} = 2 \times 10^{-6}$ s^{-1} macroscopic strain rate, there is quite a large number of grains that are deforming at lower strain rates. As a result, these grains will exhibit locally a negative SRS value leading to intermittent age hardening events which are evidenced by the PLC serrations on the stress-strain curves under the form of erratic hardening peaks of short duration on usual tensile testing machines.

Similarly, if we examine the plastic activity on the local scale of a single grain or even of a single Gauss point of the mesh inside that grain and plot the actual strain rates as a function of strain (Fig. 13) for a controlled macroscopic strain rate of 2×10^{-6} s^{-1} on the sample, large instantaneous and erratic variations are observed. The local strain rates resulting from the
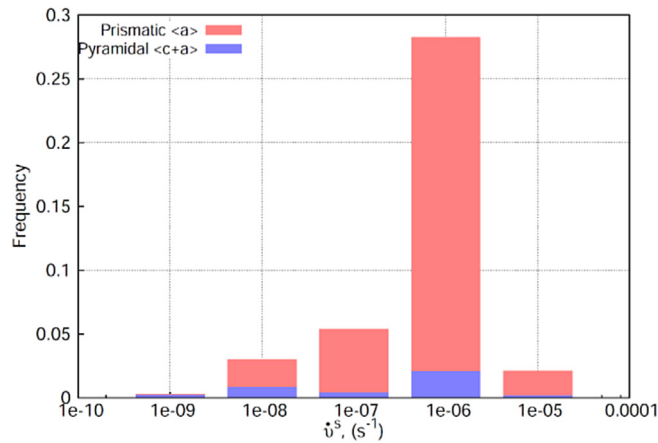

Fig. 12. Histogram of strain rates distribution in the 71 grains of the aggregates loaded at $\dot{\varepsilon} = 2 \times 10^{-6}$ s^{-1} overall strain rate and at $\varepsilon = 10\%$ overall strain in a TD oriented specimen.
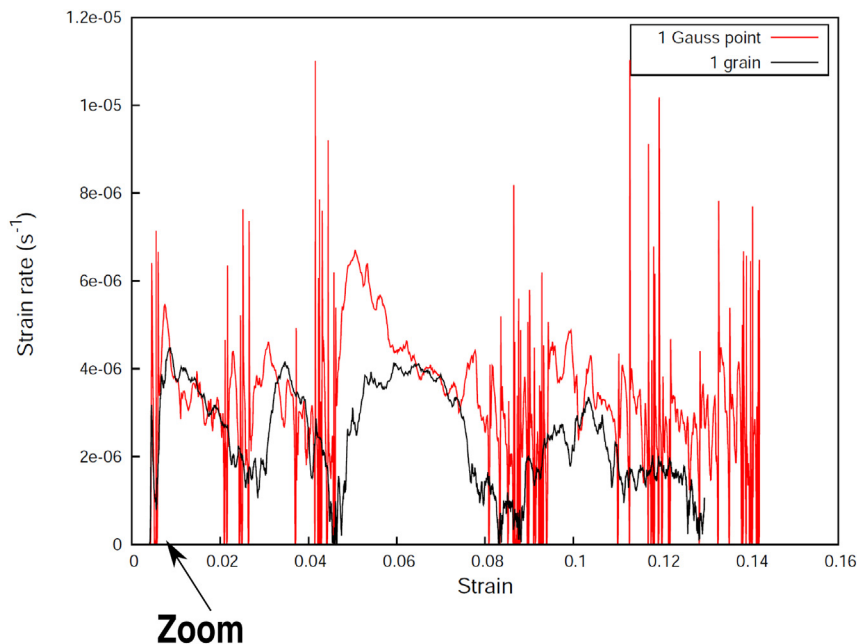

Fig. 13. Local plastic strain rate at a single material point in one grain of the FE simulation and averaged plastic strain over the whole corresponding grain as a function of total imposed overall strain. The overall strain rate is $\dot{\varepsilon} = 2 \times 10^{-6}$ s^{-1} and the tensile direction is TD.

activity of all slip systems in that grain can reach twice the macroscopically imposed strain rate or drop down to half of it or even tend to zero occasionally. As for the plastic strain rate in a single mesh of the grid (red curve in Fig. 13), it can reach 10 times the controlled strain rate or drop down to zero. This local intermittence of plasticity within a grain is confirmed by the Fig. 14 where the local strain rate is plotted as a function of time for a total strain of 0.6%, i.e. just after the yield point. Although the plastic activity for the entire grain taken on all slip systems (black curve) drops down below 2×10^{-6} s^{-1} (blue line), it never stops. On the other hand, the local plasticity in a given mesh of the FEM grid can stop completely for durations of $10-15$ min, sometimes less, but clearly allowing full aging of the activated slip systems and their necessary unlocking when the plastic activity starts again.

6. Results and discussion

6.1. Strain aging induced localization in flat extruded polycrystalline specimens

The identified polycrystalline strain aging model was used to investigate the intragranular strain and plastic strain rate instabilities that developed inside the material. The observed deformation modes differ for SSA and DSA manifestations. The results concerning SSA effects simulations are discussed first, the DSA manifestations next.

6.1.1. Examination of strain fields

The simulated macroscopic stress-strain curves for the flat polycrystalline mesh with 71 grains plotted in Fig. 15 are in good agreement with experiments. The anisotropy of the yield stress for TD and LD specimens of α Ti is well captured. The model reproduces a small yield point and plateau in TD specimens and no peak in LD specimens. The curve for a TD specimen, simulated without aging, is given in blue; the curve obtained for 'full aging' is given in purple. These two limiting curves correspond respectively to idealized test samples where the plasticity regime would be exclusively in the pure 'friction mode' (absence of age hardening) (very high strain rate), blue curve, or else in the pure 'solute drag mode' (full, permanent age hardening) (very low strain rate), purple curve. As expected, they exhibit neither yield stress anomalies, nor serrations.

Series of maps of accumulated plastic strain in the TD specimen are shown in Fig. 16 for 5 macroscopic strain levels defined in Fig. 15 with points on the stress-strain curve. Note that instead of p defined by Eq. (3), we used $\vartheta^{F(s)}$ defined by Eq. (9) presented with a logarithmic color scale. With the present numerical model we can separately examine the accumulated plastic strain on four distinct slip system families. For comparison, the total plastic strain ϑ^{total} is shown in the specimen with aging contribution (Fig. 16 (a)), next the plastic strain of prismatic <a> alone (Fig. 16 (b)) $\vartheta^{prismatic}$ and next the pyramidal <c+a> alone (Fig. 16 (c)) slip families $\vartheta^{pyramidal}$. The corresponding maps of the total plastic strain without the aging contribution are given in Fig. 16 (d). As can be seen, the 71 TD grain structure with SSA exhibits strong plastic heterogeneities, while deformation is more homogeneously distributed in space in the absence of aging. No single Lüders-like band propagation through the entire specimen was detected. Instead we observe the nucleation of local strain heterogeneities at
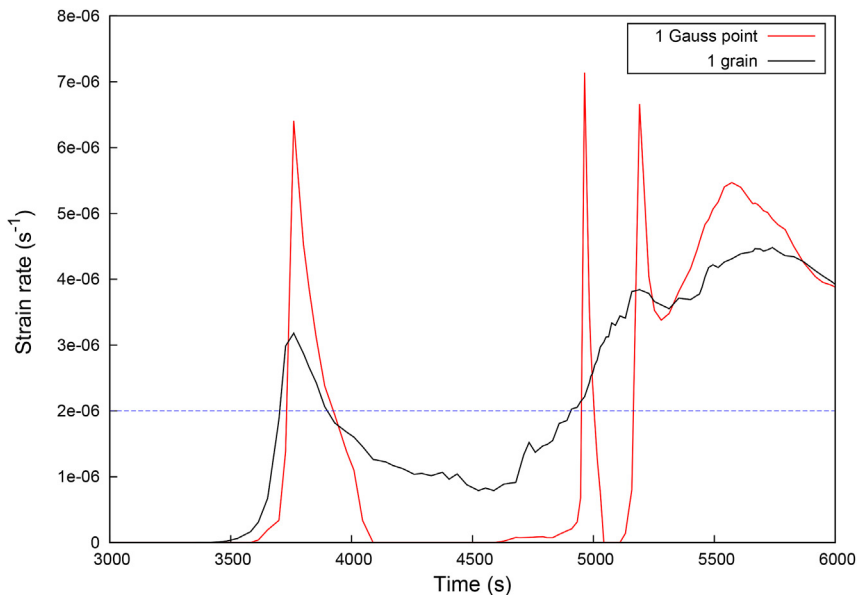

Fig. 14. Zoom at the curve of Fig. 13 at $\varepsilon_p = 0.6\%$ overall strain for a TD oriented specimen showing the sudden and drastic variations of the plastic strain rate with time inside a grain (averaged value, black curve) or at a single Gauss point belonging to this grain (red curve). (For interpretation of the references to color in this figure legend, the reader is referred to the web version of this article.)
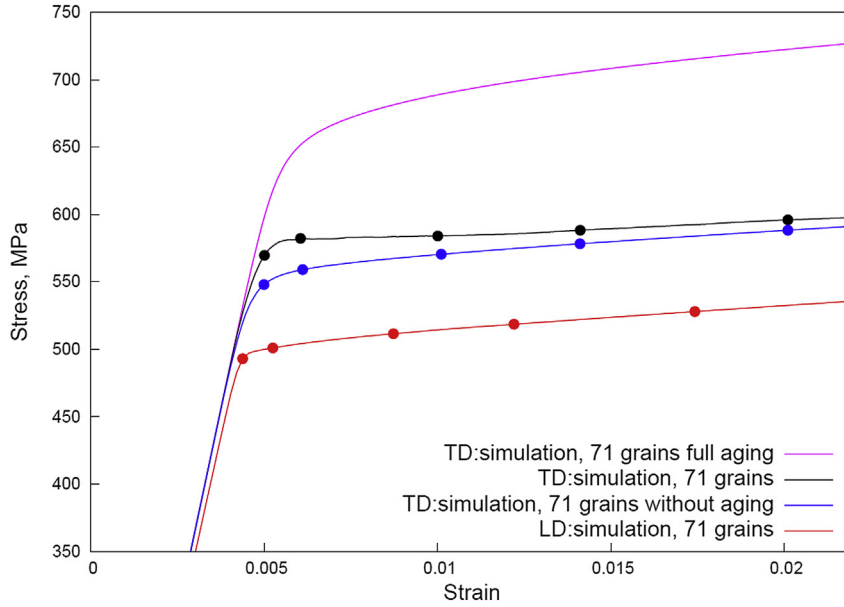
Fig. 15. Stress-strain curves of tensile simulations at $2 \times 10^{-4}\,\mathrm{s}^{-1}$ for flat extruded polycrystalline samples with 71 grains: TD, LD and TD without and with full aging effect. Selected maps for Fig. 16 are indicated by points on the corresponding curves.

multiple sites of the specimen, which later start growing and expanding over several grains cutting across grain boundaries. The observed yield point coincides with the onset of plasticity due to the activation of prismatic $<a>$ slip systems, while pyramidal $<c+a>$ slip starts later, at the onset of the plateau ($\varepsilon \approx 0.6\%$ in Fig. 16 (c)) and keeps providing a significant contribution to plasticity all along the stress-strain curve (1.6 and 2% in Fig. 16 (c)). These results are in a good agreement with experimental observations of *in-situ* tensile tests where prismatic slip was found to be a primary deformation mode for LD and TD specimens due to the lower CRSS, see Barkia et al. (2015a).

The plastic strain fields in the grains with $<a>$ prismatic slip in Fig. 16 (b) show larger gradients compared with the strong plastic band front in the grains with activated pyramidal $<c+a>$ slip systems. The plastic strain in these latter grains is mostly localized near the grain boundaries and grain boundaries triple points and only later starts filling the interior of the grain (Fig. 16(c)). In case of prismatic slip, the strain field shows less spatial inhomogeneities inside the grains.

In order to clarify the role of the pyramidal $<c+a>$ glide in the stress peak and in general on the stress-strain curve, a simulation on the 71 grain aggregate was carried out at $\dot{\varepsilon} = 2 \times 10^{-4}\,\mathrm{s}^{-1}$, in the absence of the pyramidal $\pi_1 <c+a>$ slip system family for both TD and LD orientations (dotted lines in Fig. 17) by giving an excessively high value to the CRSS of this system. It appears clearly that the $<a>$ systems alone are unable to generate a stress peak, probably due to their low age hardening ability ($r_{a_0}^{<a>} = 30$ MPa in Table 5). On the other hand, the strain softening effect provided by the unlocking of the $<c+a>$ systems in the favorably oriented grains is responsible for the stress peak and the plateau observed in the TD and for the slight decrement in flow stress and strain hardening along LD.

Note that the Lüders plateau observed in BCC materials extends over a large span of strain under an almost constant flow stress at the start of the stress-strain curve. The high symmetry of the BCC grains and large multiplicity of their slip systems with similar CRSS (including the age hardening contribution) facilitate the nucleation of plasticity and the unlocking of slip systems with little dependence on local grain orientations. In titanium, on the contrary, the presence of slip systems with significantly different CRSS and low multiplicity resulting from lower crystalline symmetry creates a scattering of the Lüders plateau, associated with $<c+a>$ pyramidal slip, all along the stress-strain curve. As evidenced by Fig. 16 (c) at $2 \times 10^{-4}\,\mathrm{s}^{-1}$ and in Fig. 23 (c) at $2 \times 10^{-6}\,\mathrm{s}^{-1}$, less favorably oriented grains progressively develop Lüders bands as the increasing flow stress of the surrounding material raises the locally applied stress to the level required to unlock the $<c+a>$ pyramidal slip. This predictive interpretation of the particular Lüders bands and plateau in α-Ti alloys remains to be confirmed by experimental micrographs including strain field mapping and slip trace analysis.

A more detailed view of the local total plastic strain localization within a couple of grains is given in Fig. 18. The strain fields formed within the grains show strain heterogeneities as large as six times the nominal strain. When strain localization starts extending into neighboring grain interiors, it still stays confined by the grain boundaries forming straining patterns which resemble deformation bands that we called meso-Lüders bands. A consequence of such cooperative grain behavior is the formation of the meso-bands inclined at about 45° for LD oriented samples.

Similarly to the TD specimen, series of maps of accumulated plastic strain in the LD specimen for 5 macroscopic strain levels are shown in Fig. 19. As in the case of the TD specimen, the total plastic strain (Fig. 19 (a)) and the plastic strain in prismatic $<a>$ (Fig. 19 (b)) and pyramidal $<c+a>$ (Fig. 19 (c)) slip families are presented separately. As expected, $<a>$ prismatic
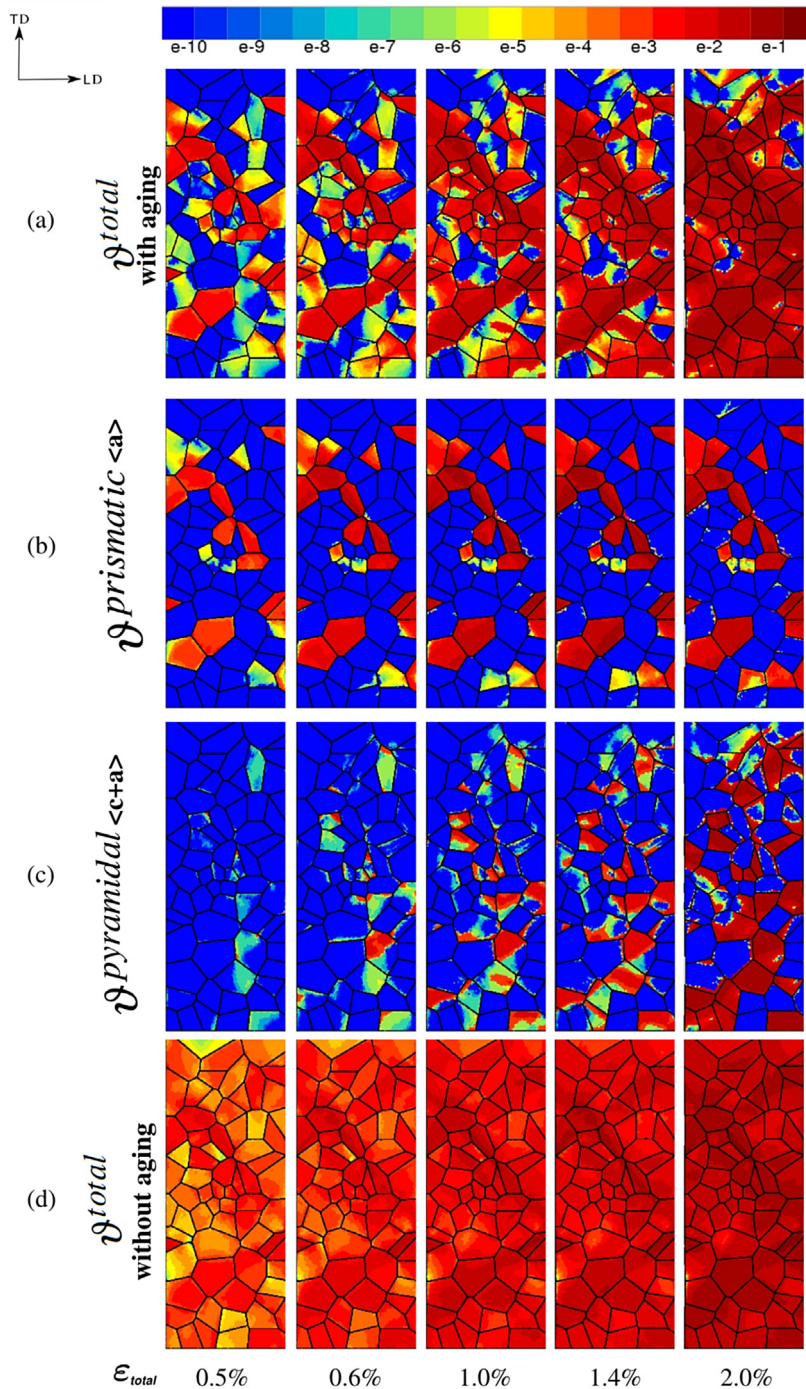
Fig. 16. Evolution of accumulated plastic strain ϑ for a flat extruded polycrystalline sample with 71 grains strained in TD at 2×10^{-4} s^{-1}: (a) total ϑ^{total}; (b) $\vartheta^{prismatic}$ on <a> slip systems; (c) $\vartheta^{pyramidal}$ on <c+a> slip systems; (d) total ϑ^{total} for the model without aging contribution.

slip is predominant, and almost no pyramidal <c+a> was activated. The total strain field remains more or less homogeneous during the tensile test simulation without formation of meso-bands, as was the case for the TD specimen.

The results of the simulations on the 432 grain TD and LD structures are given to assess the representativity of the previous observations. They are presented in Fig. 20. The TD specimen shows strong plastic heterogeneities compared with the homogeneously distributed deformation patterns in the LD specimen. Strain localization patterns are similar for both 71 and 432 grain samples. The nucleation of meso-Lüders bands in the TD specimen implies a cooperative behavior of neighboring grains.
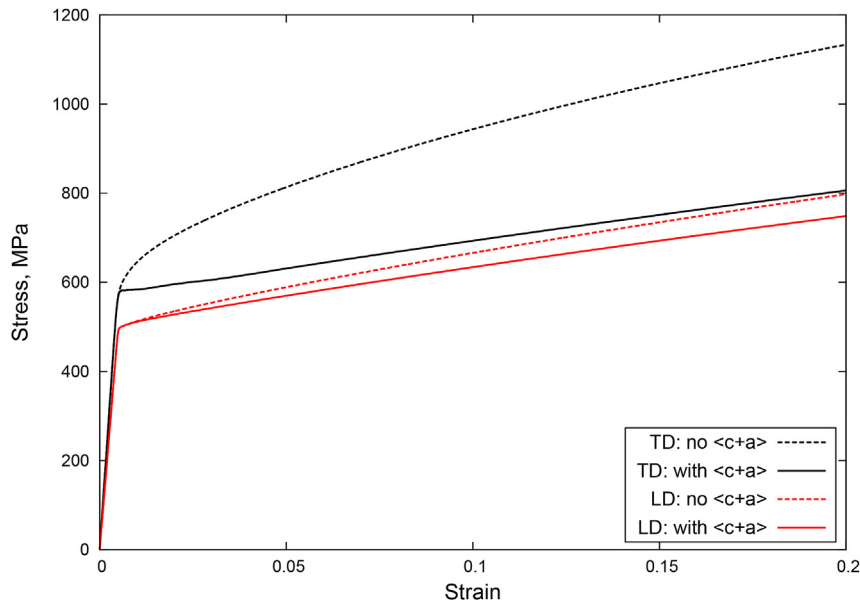
Fig. 17. Stress-strain curves of tensile simulations at $2 \times 10^{-4}\,\text{s}^{-1}$ for flat extruded polycrystalline samples with 71 grains: LD and TD with and without $<c+a>$ slip systems.

The numerical observations of the local strain fields at the mesoscale, lead to the conclusion that, in the case of SSA, the plastic shear bands can penetrate into neighboring grains when the latter are favorably oriented, they can also widen within these grains as the tensile test proceeds but will not propagate along the gauge length of the specimen by invading neighboring grains laterally as in the case of metals with high crystalline symmetry (FCC and BCC). The texture of the material favors plasticity along predetermined arrangements and associations of grains and inhibits the propagation of strain bands along the polycrystalline aggregate. This conclusion partly explains the absence of the experimental macroscopic observations of Lüders bands in α-Ti by Roth et al. (2014).

6.1.2. Examination of strain rate field maps

We now examine the strain rate maps on the flat LD and TD specimens, given by the proposed polycrystalline model including an age hardening contribution to the flow stress. Fig. 21 shows the fields of plastic strain rate $\dot{\vartheta}^{total}$ of the LD specimen and the corresponding simulation curve of the tensile test at $\dot{\varepsilon} = 2 \times 10^{-6}\,\text{s}^{-1}$. The LD specimen is of particular interest since, due to the crystal texture, we expect only $<a>$-type slip system families to contribute to the deformation. The tensile curve displays slight serrations of 2−3 MPa amplitude corresponding to the PLC effect. A series of macroscopic bands associated with the pointed stress drops on the stress-strain curve can be detected on the specimen. As can be seen in Fig. 10, the apparent macroscopic SRS remains positive in the range of applied strain rates, however locally at the level of grains, the material can exhibit negative SRS leading to DSA serrations at $\dot{\varepsilon} = 2 \times 10^{-6}\,\text{s}^{-1}$. The PLC bands nucleate at random locations along the specimen and have irregular appearance and orientation. They propagate discontinuously through the grains crossing the grain boundaries and then overlapping in some regions. They eventually cross the entire section of the sample and can be regarded as macro-PLC bands. These bands are most likely of A or possibly B-type (Lacombe, 1985b). The local total strain rate field observations in Fig. 22 show grains with intense permanent slip activity (grain A), while other grains are intermittently activated (grains B, C and D). As a result, macroscopic PLC bands are formed across grains and grain boundaries (bands number 1 and 2). The local increase in plastic strain rate precedes the band formation, and is followed by a local decrease upon disappearance of the band in a way similar to Kok et al. (2003). The separate presentation of the strain rate maps for $<a>$ slip and for $<c+a>$ slip families enables the separate identification of DSA and SSA manifestations. The quasi-absence of $<c+a>$ slip activity and its associated Lüders bands (Fig. 21 (c)) is confirmed in LD samples. In the simulations of the TD-specimen, the deformation patterns are slightly different due to the higher fraction of grains with activated $<c+a>$ type slip (see Fig. 23 (c)). As a result, we observe the combination of two deformation modes: quick periodic shear activity of the macro-PLC bands due to $<a>$ slip systems (Fig. 23 (b)) and slow permanent meso-Lüders bands thickening due to $<c+a>$ slip (Fig. 23 (c)).

The DSA simulations on the structure with 432 grains show similar localization patterns for LD and TD-specimens (see Fig. 24 (a,b)) as in the case of the 71 grain structure. The strain rate fields show large strain heterogeneities developing within grains, which later collectively develop into macroscale deformation bands that are comparable to the field measurements by Héripré et al. (2007), Raabe et al. (2001). These bands nucleate and vanish periodically and erratically, and sweep across the same region of the sample several times (Graff et al., 2004). It must be noted, that the amplitude and the frequency of serrations on the tensile curves is smaller than for 71 grains. It might be the consequence of the increased number of grains and
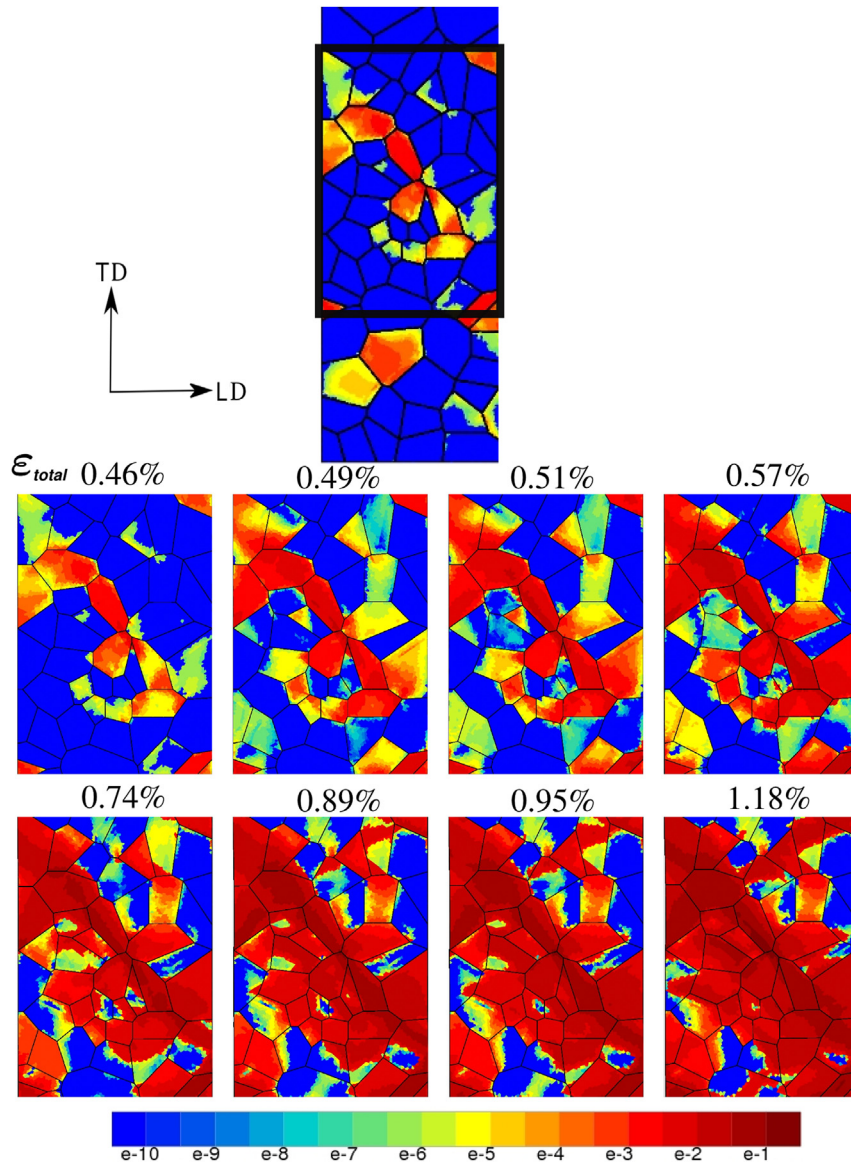
Fig. 18. Evolution of total plastic strain ϑ^{total} in a small region of a flat extruded polycrystalline sample strained at 2×10^{-4} s^{-1} along TD.

possible neighboring effect. The results of numerical simulations seem to predict the formation and propagation of macroscopic PLC bands in CP α-Ti, even though larger numbers of grains should be considered to conclude. These results are of particular interest since, to date, no experimental evidence of nucleation and propagation of macroscopic PLC bands in Ti alloys at room temperature can be found in the literature, probably because very low strain rate tests are required.

6.1.3. Optimization of critical parameters of the model

So far, the method of identification of the models parameters remains rather crude and qualitative. A quantitative tool is needed and also a larger data base of mechanical tests including creep, relaxation and cyclic testing. For instance, it is apparent that the amplitudes of the serrations obtained at 2×10^{-6} s^{-1} on TD samples, by the model in combination with the set of parameters gathered in Table 5, are too small (see insert of Fig. 10) compared with the experimental data (see insert of Fig. 4). Hence, it is interesting to examine the stress-strain curves the model would yield for a slower strain rate of 2×10^{-7} s^{-1}. Correspondingly, it would mean dividing the $t_0^{F(s)}$ parameters of the locking processes by a factor of 10. The results are presented in Fig. 25 for comparison, together with the two limiting curves corresponding to 'no aging' and 'full aging' regimes. Although the average flow stresses of both curves are identical, their positions, with respect to their respective limiting curves in the DSA domain, are different. The flow stress of the curve at 2×10^{-7} s^{-1} has a larger contribution from

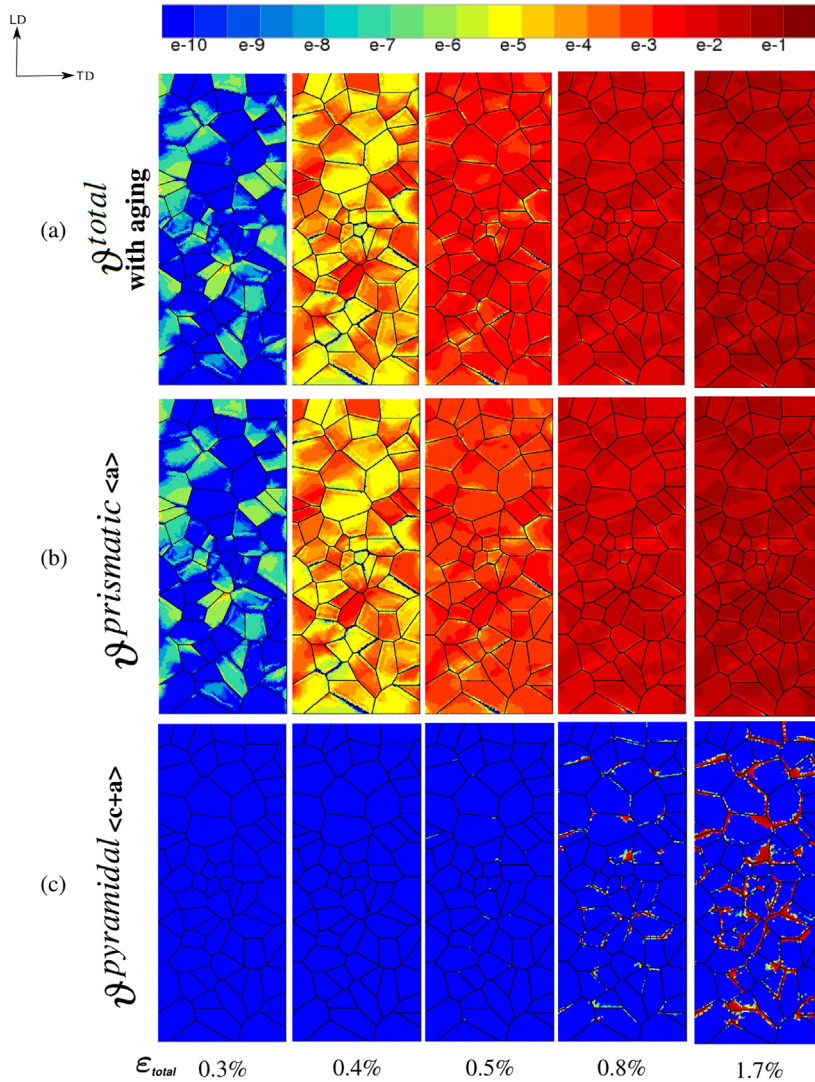**Fig. 19.** Evolution of plastic strain ϑ for flat extruded polycrystalline sample with 71 grains strained in LD at 2×10^{-4} s^{-1}: (a) total ϑ^{total}; (b) $\vartheta^{prismatic}$ on <a> slip systems; (c) $\vartheta^{pyramidal}$ on <c+a> slip systems.

aging phenomena than that of the curve at 2×10^{-6} s^{-1} and, as a consequence, it is exhibiting serrations of significantly higher amplitude.

6.1.4. Intermittence in strain rate field maps

The intermittence of collective strain rate localization events is illustrated in Fig. 26 showing the response of a 71 grain aggregate loaded in tension along TD at the strain rate of 2×10^{-7} s^{-1}. Plastic straining almost disappears when 'most of the structure' (here the tensile sample) is age hardening and the flow stress increases, which corresponds to the rising parts of the serrated tensile curve in Fig. 26, for instance at the points 2 and 4 indicated on the curve. On the contrary, when a shear band is reactivated (with a pseudo-period of 20 tp 30 mn), a sudden strain burst is accompanied with unloading of the structure, in proportion to the excess strain it is providing temporarily. Notice that the strain localization bands get reactivated, almost exactly at their previous location, meaning that hardly any sweeping is taking place across the sample.

6.2. Strain aging induced localization in 3D polycrystalline aggregates

The full 3D simulations were performed on the polycrystalline aggregate of 150 grains in order to check the validity in 3D of the phenomena observed in 2D. Fig. 27 (a,b) shows the contour maps of the accumulated plastic strain for the tension tests carried along LD and TD-specimens at $\dot{\varepsilon} = 2 \times 10^{-4}$ s^{-1} and the corresponding macroscopic stress-strain curves (Fig. 27 (c)).
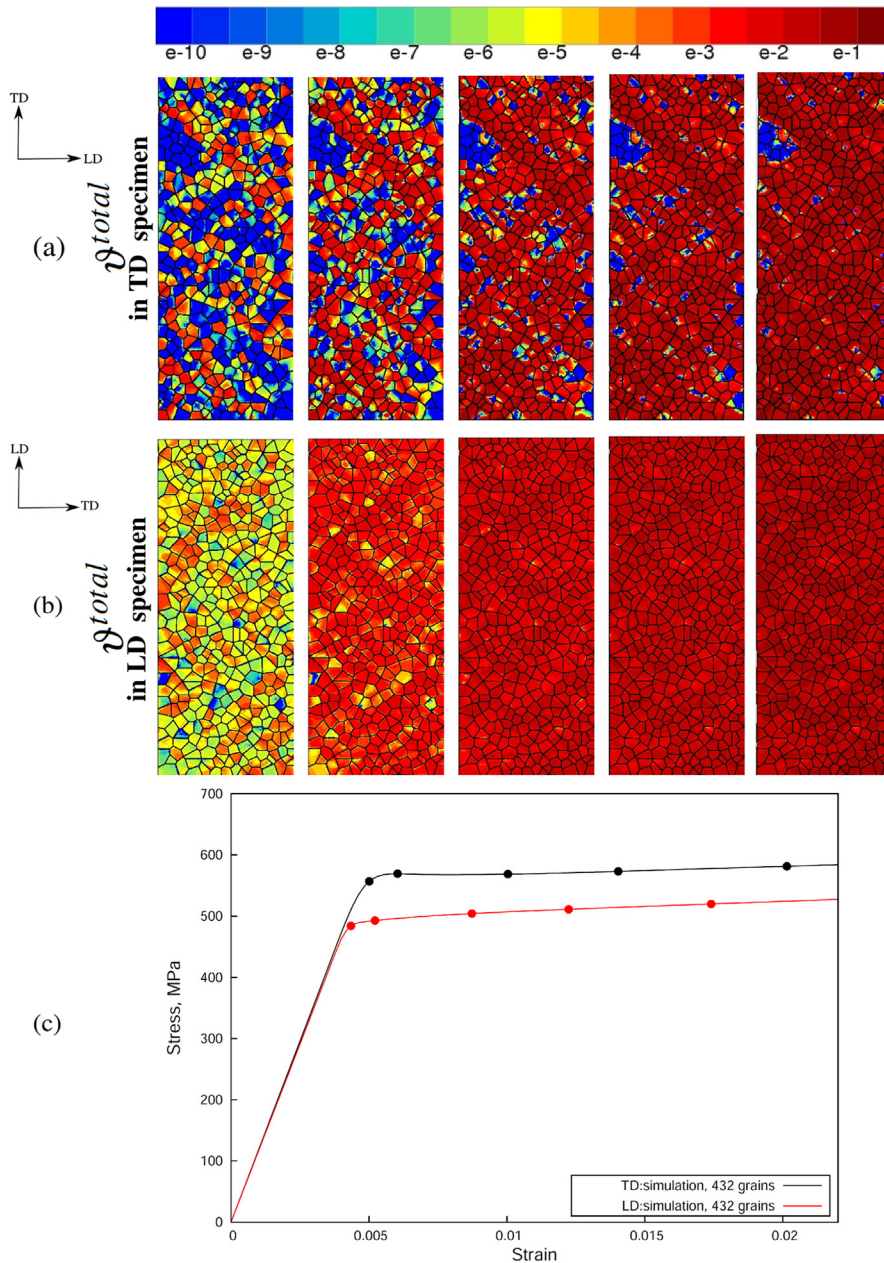
Fig. 20. Plastic strain ϑ^{total} at 2×10^{-4} s^{-1} for flat extruded polycrystalline sample with 432 grains strained in: (a) TD; (b) LD; (c) the overall stress-strained curves.

The deformation pattern of the aggregate strained along LD direction is more uniform than that of the TD-specimen. The strain field of TD-sample reveals the strain localization in the form of the shear bands across couples of grains and at the grain boundaries occurring at the moment of the yield peak on at the stress-strain curve.

The results of the DSA simulations on fully 3D aggregates at $\dot{\varepsilon} = 2 \times 10^{-6}$ s^{-1} display the same type of localization phenomena as in the case of flat extruded specimens, but it is more difficult to observe due to the coarseness of the FE mesh used. The comparison of the experimental and simulation results obtained on flat extruded polycrystalline specimens and fully 3D aggregates show the correctly predicted anisotropy of the mechanical behavior of CP α-Ti. The set of identified parameters adequately simulates the anomalous yield point for TD-specimen in 2D as well as in 3D. The PLC effect was reproduced on TD and LD-specimens at 2×10^{-6} s^{-1}, even though the model should be improved to better describe the detailed evolution, especially the frequency and the amplitude of the serrations. One possibility to increase the amplitude of serrations as mentioned above is to shift the parameter t_0^s of each system s to slightly smaller values (5 s and 50 s for <a> and <c+a>
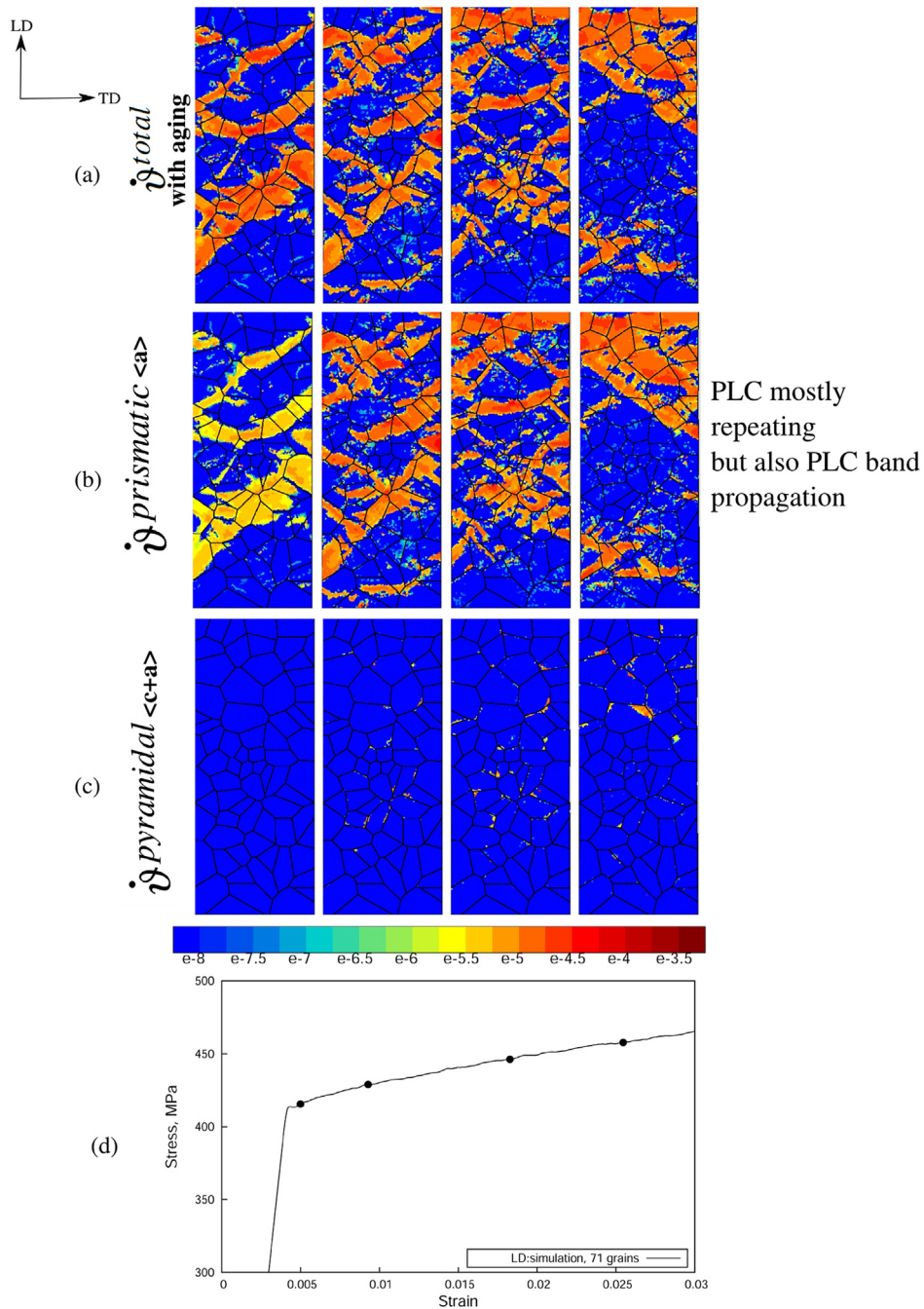
Fig. 21. Accumulated plastic strain rate $\dot{\vartheta}$ for flat extruded polycrystalline 71 grain sample strained in LD at 2×10^{-6} s^{-1}: (a) total $\dot{\vartheta}^{total}$; (b) $\dot{\vartheta}^{prismatic}$ on $<a>$ slip systems; (c) $\dot{\vartheta}^{pyramidal}$ on $<c+a>$ slip systems; (d) the corresponding overall stress-strain curve.

respectively instead of 10 s and 100 s, see Table 5). The other possibility would be to include in the model the stiffness of the testing machine, which was shown to amplify the DSA effect by Wang et al. (2012). Both options should be tried. The numerical results obtained so far support the proposed scenario for the plastic instabilities observed in CP α-Ti.

6.3. Shortcomings of the model

The constitutive model presented in this paper is based on a number of estimated assumptions necessary to keep it as simple as possible. The new ingredients were limited to the introduction of one aging time variable per slip system family, the
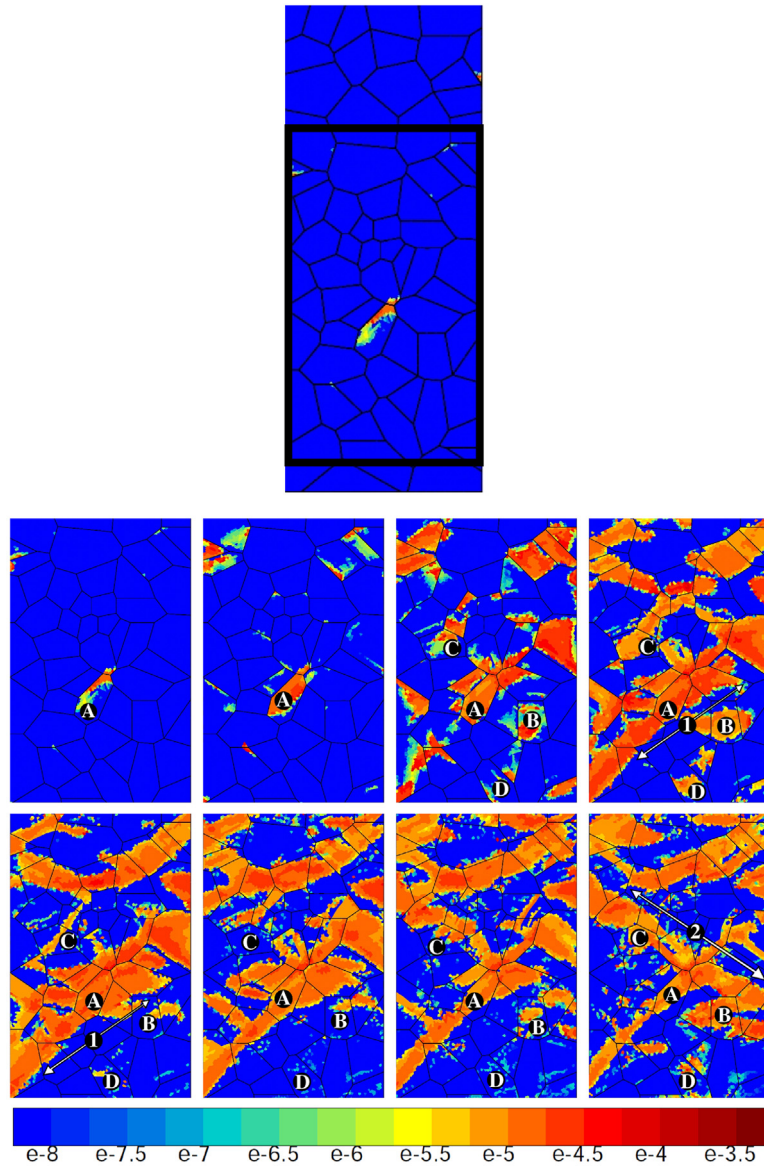
Fig. 22. Evolution of total plastic strain rate $\dot{\vartheta}^{total}$ for flat extruded polycrystalline sample with 71 grains strained in LD at 2×10^{-6} s^{-1}. Grain A exhibits quasi permanent plasticity, whereas grains B, C and D experience intermittent activity. Intermittent bands labeled '1' and '2' can evolve in several grains.

number of parameters was kept minimal and we paid attention to their mechanical and/or physical meaning. Among the most obvious shortcomings of the model, the following can be mentioned:

- The stiffness/frequency response of the testing machine was ignored; yet in the presence of localized avalanches of plasticity (also called strain bursts by Fressengeas et al. (2005)) due to SSA and DSA phenomena, the detailed understanding of the stress/strain curves (shape, amplitude and frequency of stress peaks, serrations) must include the dynamic response of the testing machine.
- Isotropic hardening was assumed for simplicity and may be acceptable as a first order approach in the low temperature/ high strain rate part of the PLC domain for Ti based alloys tested in a monotonic uni-axial manner. At higher temperature and/or in fatigue test, cyclic relaxation and creep tests with periodic load changes, it would become necessary to introduce a kinematic hardening term and a temperature dependant restoration term.
- The crystallographic textures used so far in the model are statistically equivalent or approaching the experimentally recorded ones but the local distribution of crystalline orientations of neighboring grains is not accounted for. Since the local orientations of grains and their mutual arrangement determine the shape and the extent of strain and strain rate
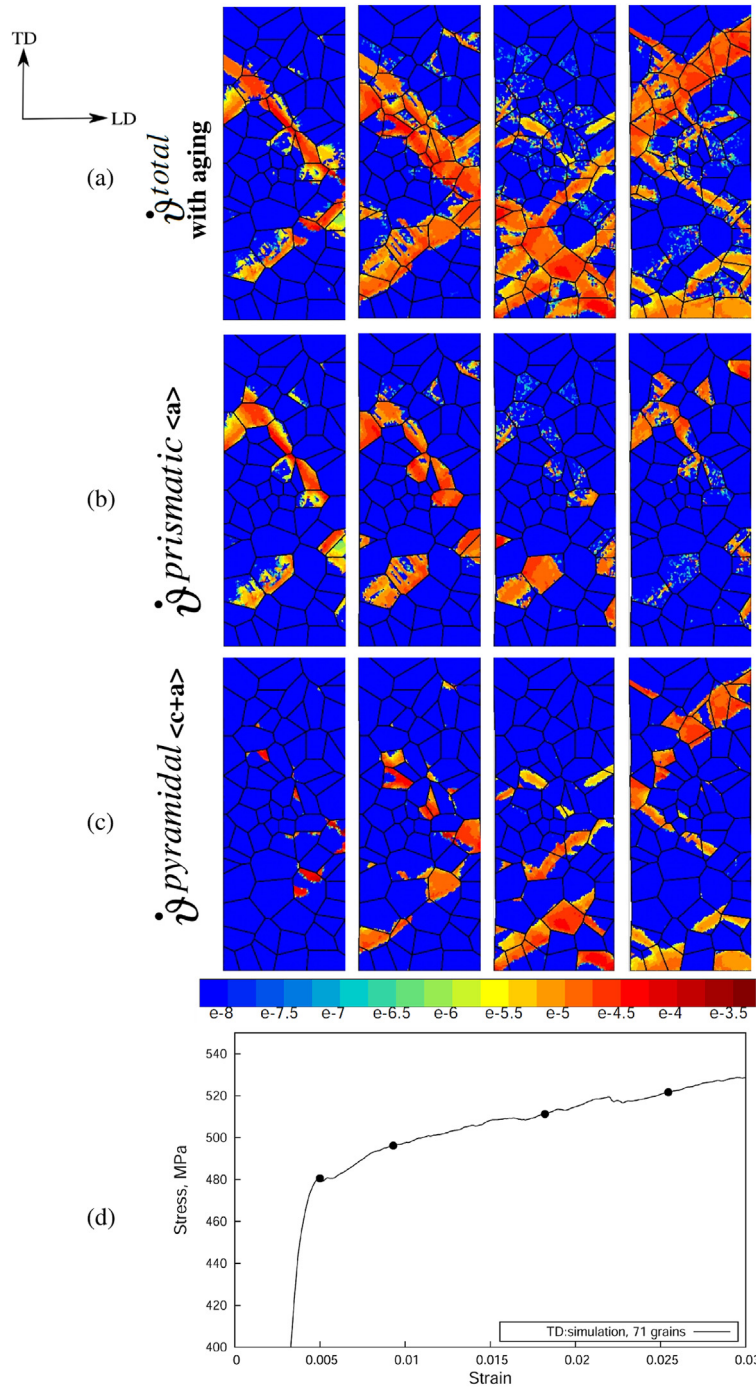
Fig. 23. Accumulated plastic strain rate $\dot{\vartheta}$ for flat extruded polycrystalline 71 grain sample strained in TD at 2×10^{-6} s^{-1}: (a) total $\dot{\vartheta}^{total}$; (b) $\dot{\vartheta}^{prismatic}$ on $<a>$ slip systems; (c) $\dot{\vartheta}^{pyramidal}$ on $<c+a>$ slip systems; (d) the corresponding overall stress-strain curve.

localization bands, it must be taken into account by use a local grain arrangement imitating EBSD maps of actual flat samples taken from a rolled sheet material.

• The complete lack of quantitative experimental data regarding the level of interactions between slip systems is preventing the determination of self and cross-hardening coefficients in Eq. (7). Similarly, the formation of dislocation networks or cell walls with long range stress fields (kinematic hardening) or without (isotropic hardening) is not well documented, yet, in the literature concerning HCP materials.
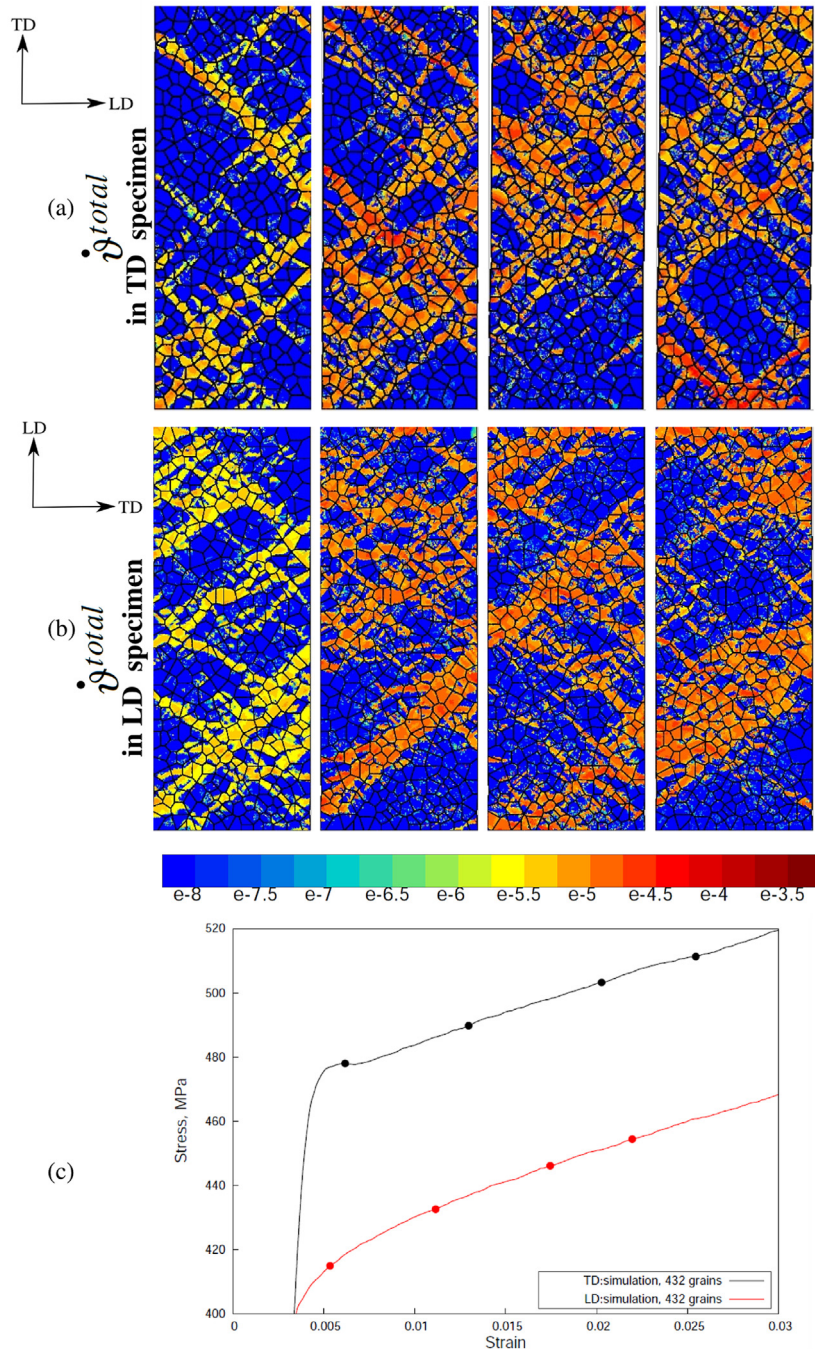
Fig. 24. Equivalent plastic strain rate $\dot{\vartheta}^{total}$ for flat extruded polycrystalline sample with 432 grains strained at 2×10^{-6} s^{-1} in: (a) TD; (b) LD; (c) the overall stress-strain curves.

The rationale behind the choice of parameters and coefficients requested by the model was exposed in 5.2–5.4 and summarized in Table 5. The shortcomings just mentioned must be kept in mind and foster an attitude of caution when trying to interpret the results in great detail.

7. Conclusions

In the present study, we investigated the phenomena of static and dynamic strain aging in cold-rolled CP α-Ti using computational mechanics of polycrystals. The physical mechanisms underlying the existence of strain heterogeneities in CP
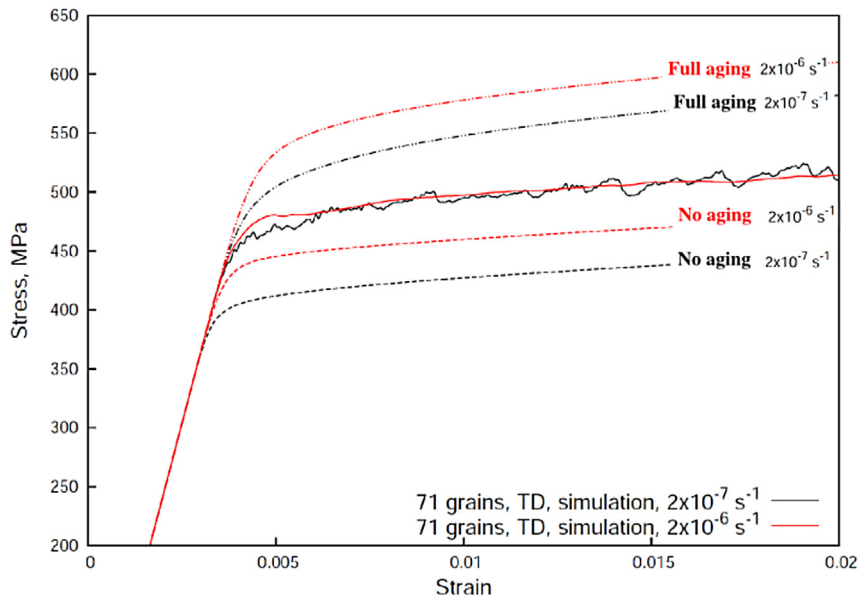
Fig. 25. Stress-strain curves of tensile simulations at 2×10^{-6} s^{-1} (red curves) and 2×10^{-7} s^{-1} (black curves) for flat extruded polycrystalline samples with 71 grains in TD without and with full aging effect. (For interpretation of the references to color in this figure legend, the reader is referred to the web version of this article.)

α-Ti were reviewed. The origin of the anomalous yield point phenomenon in the samples strained along TD was attributed to the interaction of $<c+a>$ dislocations with interstitial atoms of oxygen. The PLC effect exhibited by TD and LD-specimens was ascribed to the ability of $<a>$ screw dislocations with the non-planar core structure to recombine into various slip planes and thus change from sessile into glissile core configurations capable of easy cross-slip.

Based on the proposed scenario, a new phenomenological elastic-viscoplastic aging model coupled with crystal plasticity was proposed to simulate the SSA and DSA effects. The FEM simulations were carried out for various specimens in tension: on flat extruded polycrystalline specimens and on full 3D samples. The presented identification method enables calibration of viscosity, hardening and aging parameters.

In the case of SSA, the FEM simulations of tensile tests give a satisfactory description of the stress-strain curves with a correct prediction of the material anisotropy resulting from the crystallographic texture. As in the experiments, the TD simulation curves show slight yield peak followed by a stress plateau. The examination of strain field simulations reveals the presence of complex plastic strain localization phenomena at work inside and across the grains. They take place within specific assemblies of grains which are sharing crystalline orientations rather favorable for plasticity and therefore tend to retain and concentrate plastic strain. Thus, contrary to the usual Lüders bands (observed on pure iron, for instance) that easily extend to neighboring grains and propagate across grain boundaries, the strain localization bands generated by the present numerical model appear fairly immobile because they are anchored by the crystalline texture. We suggest calling them meso-Lüders bands. Such locally persistent straining patterns were recently observed experimentally by Barkia (2014) in this material.

The resulting overall stress-strain curves of the DSA simulations show slight serrations on both TD and LD specimens corresponding to the PLC effect. The numerical model predicts initiation and propagation of macroscopic PLC bands in the explored strain rate domain. These mesoscopic bands are formed due to the cooperative behavior of the grains, where the strain is localized. PLC serrations were obtained even in the presence of a positive value of the macroscopic SRS, as in the experiment.

In addition to the standard strain hardening terms, a time dependent hardening term was added to the flow stress which enables time and space decoupled aging events to take place within the structure. The model recognizes the crystalline nature of the mechanical structure by the use of the identified slip systems and takes into account the lower symmetry of the HCP crystals constitutive of CP α Ti, as compared with FCC or BCC crystals of higher symmetry. As a consequence, local strain softening events may occur, associated with strain localization patterns and local strain rates in large excess to the nominal macroscopic strain rate. For rather small spatial extension of these plastic avalanches and when these events concern only a minor volume fraction of the entire sample, the amplitude of the serrations, on the stress-strain curves, remain small and compatible with a positive value of the macroscopic SRS of the sample. This apparent discrepancy between local, micro-scale value of the SRS and its macro-scale value was observed and well simulated here, at room temperature, in the low temperature (or high strain rate) region of the PLC domain of this material. An additional achievement of this model is to provide for SSA as well as for DSA strain localization bands, by its appropriate crystalline description of the material, a clear
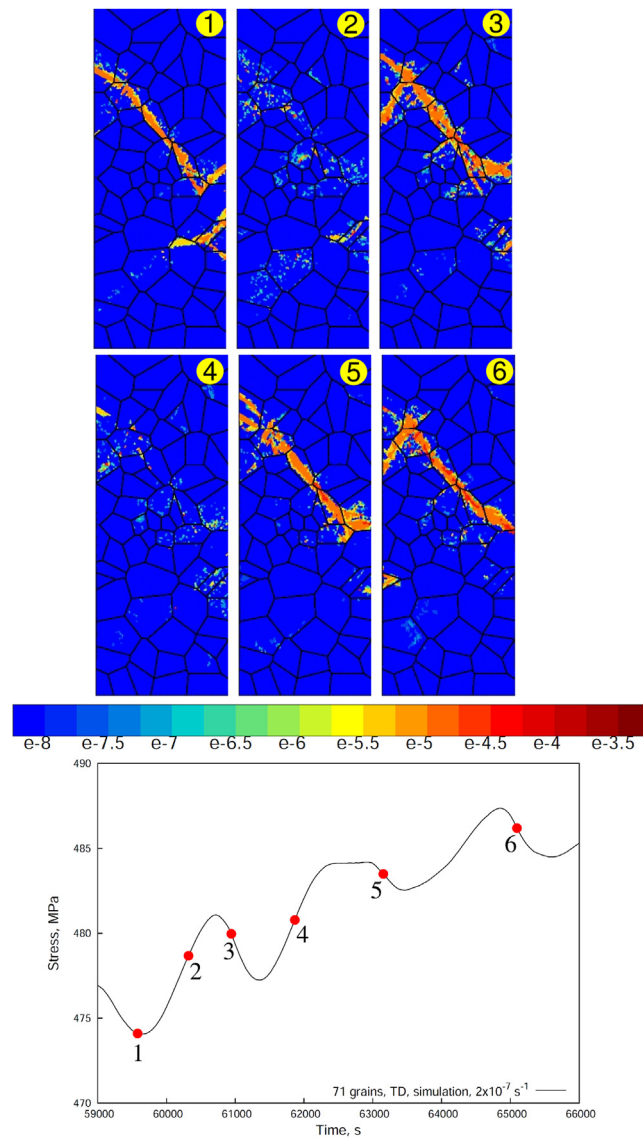
Fig. 26. Equivalent plastic strain rate $\dot{\vartheta}^{total}$ for flat extruded polycrystalline sample with 71 grains strained at 2×10^{-7} s^{-1} in TD.

interpretation of the lack of mobility or the absence of plastic fronts in this material, in contrast with their counterparts, usually observed in Fe or Al based alloys, which appear highly mobile and able to cross easily all grain boundaries.

In the future, experiments at lower strain rates should be performed in order to confirm (or not) the numerically predicted PLC bands. One of the further step for this study will be to perform actual 3D crystal plasticity computations based on real grain shapes, orientations and actual neighborhood of grains (as given by EBSD maps) of real samples in order to accurately determine the local mechanical field in polycrystalline materials as well as stress-strain heterogeneities developing in grains during deformation. Such a comparison between experimental and computational results would be the most appropriate validation of the proposed theory and evidence of the strain aging phenomena taking place at the grain scale. However, two major difficulties are encountered. The first one deals with the well-known fact that the knowledge of the surface morphology and orientation of grains is not sufficient for a reliable prediction of surface plastic deformation by means of crystal plasticity. The shape of the grains below the surface must be known, as demonstrated in papers by Zeghadi et al. (2007), Zhao et al. (2008). The second difficulty deals with accurate strain (or temperature) field measurements at the grain scale able to detect plastic intermittence associated with SSA and DSA. The amplitude of the events predicted by the computations is rather small and would require very accurate measurements. This is practically possible thanks to recent measurements methods, for example by Charkaluk et al. (2014); Guery et al. (2016). The combination of these techniques is a challenging next step in the study of strain aging phenomena in polycrystals. Note that a first step has already been
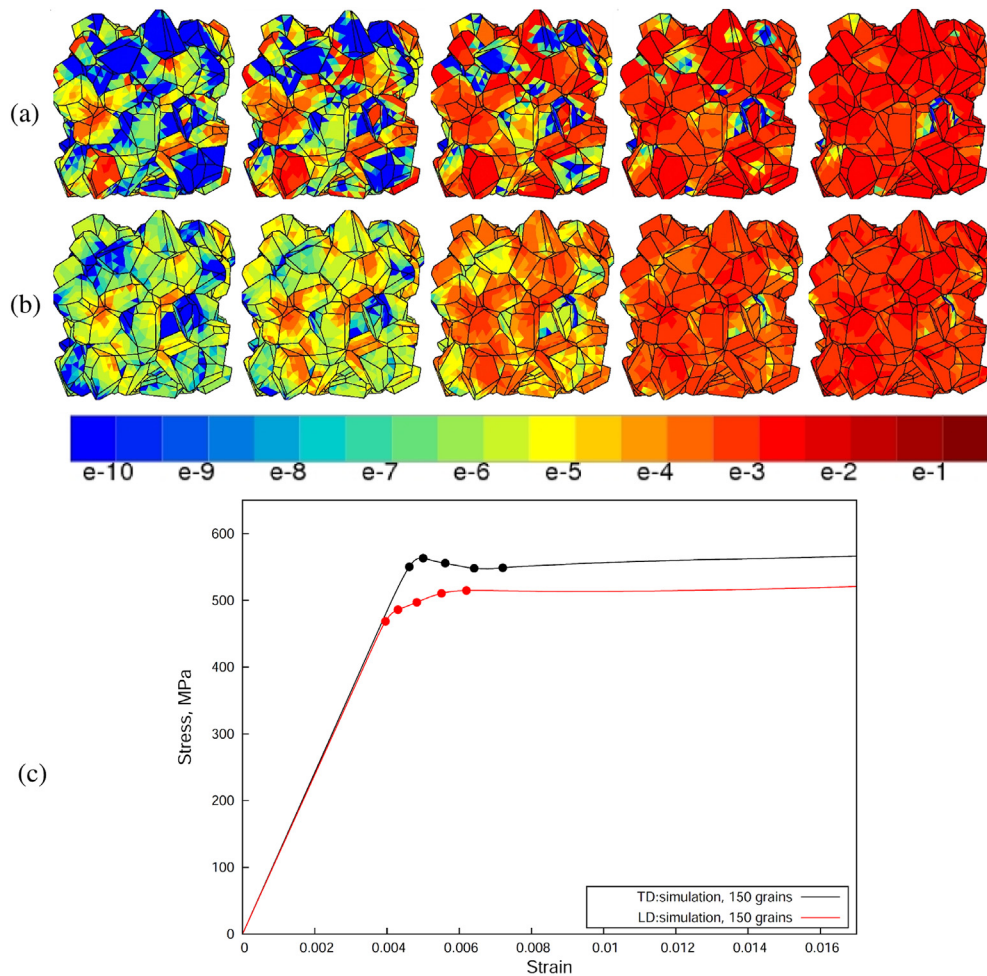
Fig. 27. Evolution of accumulated total plastic strain ϑ^{total} of a 3D polycrystalline aggregate during a tensile test at $\dot{\varepsilon} = 2 \times 10^{-4}$ s^{-1} for: (a) TD, (b) LD, (c) corresponding stress-strain curves.

accomplished by Barkia et al. (2015b) where EBSD and DIC in situ measurements in a SEM were combined to measure the strain field in the same material as in the present work. These measurements during tensile tests performed in a SEM along the rolling and transverse directions confirm the formation of long highly-deformed bands inclined at about 45° to the LD in the early stages of plastic flow. It was also observed that, as the deformation proceeds, these bands start expanding, but remain located in the same zone.

Acknowledgments

References

Alankar, A., Eisenlohr, P., Raabe, D., 2011. Dislocation density-based crystal plasticity constitutive model for prismatic slip in α-titanium. Acta Mater. 59, 7003—7009.

Amouzou, K.E.K., Richeton, T., Roth, A., Lebyodkin, M., Lebedkina, 2016. Micromechanical modeling of hardening mechanisms in commercially pure α-titanium in tensile condition. Int. J. Plasticity 80, 222—240.

Barbe, F., Decker, L., Jeulin, D., Cailletaud, G., 2001a. Intergranular and intragranular behavior of polycrystalline aggregates. Part 1: F.E. model. Int. J. Plasticity 17, 513—536.

Barbe, F., Forest, S., Cailletaud, G., 2001b. Intergranular and intragranular behavior of polycrystalline aggregates. Part 2: results. Int. J. Plasticity 17, 537—563.

Barkia, B., 2014. Viscoplasticité à l'ambiante du titane en relation avec ses teneurs en oxygène et hydrogène. Ecole Polytechnique. Ph.D. thesis.

Barkia, B., Doquet, V., Couzinié, J., Guillot, I., Héripré, E., 2015a. In situ monitoring of the deformation mechanisms in titanium with different oxygen contents. Mater. Sci. Eng. A 636, 91—102.

Barkia, B., Doquet, V., Héripré, E., Guillot, I., 2015b. Characterization and analysis of deformation heterogeneities in commercial purity titanium. Mater. Charact. 108, 94–101. http://www.sciencedirect.com/science/article/pii/S1044580315003290. http://dx.doi.org/10.1016/j.matchar.2015.09.001.

Battaini, M., 2008. Deformation Behavior and Twinning Mechanisms of Commercially Pure Titanium Alloys. Monash Universtity. Ph.D. thesis.

Benallal, A., Berstad, T., Borvik, T., Clausen, A., Hopperstad, O., 2006. Dynamic strain aging and related instabilities: experimental, theoretical and numerical aspects. Eur. J. Mech. 25, 397–424.

Berveiller, M., Zaoui, A., 1978. An extension of the self-consistent scheme to plastically-flowing polycrystals. J. Mech. Phys. Solids 26, 325–344.

Besson, J., Cailletaud, G., Chaboche, J.L., Forest, S., 2010. Non-linear Mechanics of Materials. In: Solid Mechanics and its Applications, vol. 167. Springer.

Bharathi, M., Lebyodkin, M., Ananthakrishna, G., Fressengeas, C., Kubin, L., 2002. The hidden order behind jerky flow. Acta Mater. 50, 2813–2824.

Biget, M.P., Saada, G., 1989. Low-temperature plasticity of high-purity α-titanium single crystals. Philos. Mag. A 59, 747–757.

Brandes, M., Mills, M., 2004. Static recovery in titanium alloys at lower temperatures. Mater. Sci. Eng. A 387–389, 570–575.

Bridier, F., Villechaise, P., Mendez, J., 2005. Analysis of the different slip systems activated by tension in a α–β titanium alloy in relation with local crystallographic orientation. Acta Mater. 53, 555–567.

Caillard, D., Couret, A., 2002. Dislocation movements controlled by friction forces and local pinning in metals and alloys. Mater. Sci. Eng. A 322, 108–117.

Caillard, D., Martin, J., 2003. Thermally Activated Mechanisms in Crystal Plasticity. In: Pergamon Materials Series, vol. 8. Pergamon.

Cailletaud, G., 1992. A micromechanical approach to inelastic behaviour of metals. Int. J. Plasticity 8, 55–73.

Cailletaud, G., Diard, O., Feyel, F., Forest, S., 2003. Computational crystal plasticity: from single crystal to homogenized polycrystals. Tech. Mech. 23, 130–145.

Chaboche, J., Gaubert, A., Kanoute, P., Longuet, A., Azzouz, F., Mazière, M., 2013. Viscoplastic constitutive equations of combustion chamber materials including cyclic hardening and dynamic strain aging. Int. J. Plasticity 46, 1–22.

Charkaluk, E., Seghir, R., Bodelot, L., Witz, J.F., Dufrénoy, P., 2014. Microplasticity in polycrystals: a thermomechanical experimental perspective. Exp. Mech. 55, 741–752. http://dx.doi.org/10.1007/s11340-014-9921-z.

Cho, S., Chasiotis, I., 2007. Elastic properties and representative volume element of polycrystalline silicon for MEMS. Exp. Mech. 47, 37–49.

Clouet, E., 2012. Screw dislocation in zirconium: Ab-initio study. Phys. Rev. B 86, 144104.

Colas, D., Finot, E., Flouriot, S., Forest, S., Mazière, M., Paris, T., 2014. Investigation and modeling of the anomalous yield point phenomenon in pure tantalum. Mater. Sci. Eng. A 615, 283–295.

Conrad, H., 1981. Effect of interstitial solutes on the strength and ductility of titanium. Prog. Mater. Sci. 26, 123–403.

Cordero, N.M., Forest, S., Busso, E.P., 2012. Generalised continuum modelling of grain size effects in polycrystals. Compt. Rend. Mécanique 340, 261–274.

Couret, A., Caillard, D., 1991. Dissociations and friction forces in metals and alloys. J. de Physique III (1), 885–907.

Doner, M., Conrad, H., 1973. Deformation mechanisms in commercial Ti-50A (0.5 at.pct O)$_{eq}$ at intermediate and high temperatures (0.3–0.6 Tm). Metall. Trans. 4, 2809–2817.

Donoso, J., Reed-Hill, R., 1977. Static strain-aging in commercial purity α titanium. Metall. Trans. A 8, 945–948.

Doquet, V., Barkia, B., 2015. A micromechanical model of the viscoplastic behaviour of titanium accounting for its anisotropic and strain-rate-dependent viscosity. Mech. Time Depend Mater. 19, 153–166.

Efstathiou, C., Sehitoglu, H., Lambros, J., 2010. Multiscale strain measurements of plastically deforming polycrystalline titanium: role of deformation heterogeneities. Int. J. Plasticity 26, 93–106.

Escaig, B., 1968. L'activation thermique des déviations sous faibles contraintes dans les structures h.c. et c.c. Phys. Status Solidi B 28, 463–474.

Evans, J., Douthwaite, R., 1973. Snoek ordering and rapid strain ageing in iron-nitrogen alloys. Acta Metall. 21, 49–54.

Farenc, S., Caillard, D., Couret, A., 1993. An in situ study of prismatic glide in α-titanium at low temperatures. Acta Metall. Mater. 41, 2701–2709.

Farenc, S., Caillard, D., Couret, A., 1995. A new model for the peak of activation area of α-titanium. Acta Metall. Mater. 43, 3669–3678.

Fisher, E., Renken, D., 1964. Single-crystal elastic moduli and the hcp-bcc transformations in Ti, Zr and Hf. Phys. Rev. 135, 482–494.

Flowers, J.W., O'Brien Jr., K., McEleney, P., 1964. Elastic constants of alpha titanium single crystals of 25 °C. J. Less Common Metals 393–395.

Fressengeas, C., Beaudoin, A., Lebyodkin, M., Kubin, L., Estrin, Y., 2005. Dynamic strain aging: a coupled dislocation-solute dynamic model. Mater. Sci. Eng. A 400–401, 226–230.

Friedel, J., 1964. Dislocations. Addison-Wesley.

Garde, A., Santhanam, A., Reed-Hill, R., 1972. The significance of dynamic strain aging in titanium. Acta Metall. 20, 215–220.

Ghazisaeidi, M., Trinkle, D., 2012. Core structure of a screw dislocation in Ti from density functional theory and classical potentials. Acta Mater. 60, 1287–1292.

Gong, J., Wilkinson, A., 2009. Anisotropy in the plastic flow properties of single-crystal α titanium determined from micro-cantilever beams. Acta Mater. 57, 5693–5705.

Graff, S., Forest, S., Strudel, J., Prioul, C., Pilvin, P., Béchade, J.L., 2005. Finite element simulations of dynamic strain ageing effects at V-notches and crack tips. Scr. Mater. 52, 1181–1186.

Graff, S., Forest, S., Strudel, J., Prioul, C., Pilvin, P., Béchade, J.L., 2004. Strain localization phenomena associated with static and dynamic strain ageing in notched specimens: experiments and finite element simulations. Mater. Sci. Eng. A 387–389, 181–185.

Guery, A., Hild, F., Latourte, F., Roux, S., 2016. Slip activities in polycrystals determined by coupling DIC measurements with crystal plasticity calculations. Int. J. Plasticity 81, 249–266. http://www.sciencedirect.com/science/article/pii/S0749641916000188. http://dx.doi.org/10.1016/j.ijplas.2016.01.008.

Guillot, I., Feaugas, X., Clavel, M., 2001. Dislocation–hydride interaction at low plastic strain in titanium. Scr. Metall. 44, 1011–1017.

Héripré, E., Dexet, M., Crépin, J., Gélébart, L., 2007. Coupling between experimental measurements and polycrystal finite element calculations for micromechanical study of metallic materials. Int. J. Plasticity 23, 1512–1539.

Hull, D., Bacon, D.J., 1984. Introduction to Dislocations. Pergamon.

Jousset, H., 2008. Viscoplasticité et microstructures d'un alliage de titane: effects de la temperature et de la vitesse de sollicitation. Ecole des Mines de Paris. Ph.D. thesis.

Keeler, J., Geisler, A., 1957. Preferred orientations in rolled and annealed titanium. J. Metals 206, 80–90.

Kelly, P., Smith, P., 1973. Strain-ageing in zirconium-oxygen alloys. J. Nucl. Mat. 46, 23–34.

Kok, S., Bharathi, M., Beaudoin, A., Fressengeas, C., Ananthakrishna, G., Kubin, L., Lebyodkin, M., 2003. Spatial coupling in jerky flow using polycrystal plasticity. Acta Mater. 51, 3651–3662.

Kubin, L., Estrin, Y., 1985. The Portevin-Le Chatelier effect in deformation with constant stress rate. Acta Metall. 33, 397–407.

Kubin, L., Estrin, Y., 1991. Dynamic strain ageing and the mechanical response of alloys. J. de Physique III (1), 929–943.

Kubin, L., Estrin, Y., Perrier, C., 1992. On static strain ageing. Acta Metall. Mater. 40, 1037–1044.

Lacombe, P., 1985a. Influence of impurities on the mechanical properties of titanium and titanium alloys, in: Titanium'84: science and technology. In: 5th Proceedings of the World Conference on Titanium, pp. 2705–2721.

Lacombe, P., 1985b. L'effet Portevin-Le Chatelier, ses caractéristiques et ses conséquences sur les hétérogénéités de déformation plastique. Matériaux Tech. 73, 5–15.

Lebedkina, T., Lebyodkin, M., 2008. Effect of deformation geometry on the intermittent plastic flow associated with the Portevin-Le Chatelier effect. Acta Mater. 56, 5567–5574.

Legrand, B., 1984. Influence de la structure électronique sur la facilité relative des glissements dans les métaux de structure hexagonale compacte. Université Pierre et Marie Curie. Ph.D. thesis.

Li, H., Boehlert, C., Bieler, T., Crimp, M., 2012. Analysis of slip activity and heterogeneous deformation in tension and tension-creep of Ti-5Al-2.5Sn (wt %) using in-situ SEM experiments. Philos. Mag. 92, 2923–2946.

Li, H., Mason, D., Bieler, T., Boehlert, C., Crimp, M., 2013. Methodology for estimating the critical resolved shear stress ratios of α-phase Ti using EBSD-based trace analysis. Acta Mater. 61, 7555–7567.

Lütjering, G., Williams, J., 2007. Titanium. Springer.

Marais, A., Mazière, M., Forest, S., Parrot, A., Le Delliou, P., 2012. Identification of a strain-aging model accounting for Lüders behavior in a C-Mn steel. Philos. Mag. 92, 3589–3617.

Mazière, M., Besson, J., Forest, S., Tanguy, B., Chalons, H., Vogel, F., 2010. Numerical aspects in the finite element simulation of the Portevin-Le Chatelier effect. Comput. Methods Appl. Mech. Eng. 199, 734–754.

McCormick, P., 1988. Theory of flow localization due to dynamic strain ageing. Acta Metall. 36, 3061–3067.

Mesarovic, S., 1995. Dynamic strain aging and plastic instabilities. J. Mech. Phys. Solids 43, 671–700.

Musienko, A., Cailletaud, G., 2009. Simulation of inter- and transgranular crack propagation in polycrystalline aggregates due to stress corrosion cracking. Acta Mater. 57, 3840–3855.

Naka, S., 1983. Etude des mecanismes de déformation plastique a basse temperature de monocristaux de titane α. Université d'Orsay. Ph.D. thesis.

Naka, S., Kubin, L.P., Perrier, C., 1991. The plasticity of titanium at low and medium temperatures. Philos. Mag. A 63, 1035–1043.

Naka, S., Lasalmonie, A., Costa, P., Kubin, L.P., 1988. The low-temperature plastic deformation of α-titanium and the core structure of a-type screw dislocations. Philos. Mag. A 57, 717–740.

Nemat-Nasser, S., Guo, W., Cheng, J., 1999. Mechanical properties and deformation mechanisms of a commercially pure titanium. Acta Mater. 47, 3705–3720.

Nixon, M.E., Cazacu, O., Lebensohn, R.A., 2010. Anisotropic response of high-purity a-titanium: experimental characterization and constitutive modeling. Int. J. Plasticity 26, 516–532.

Osipov, N., Gourgues-Lorenzon, A.F., Marini, B., Mounoury, V., Nguyen, F., Cailletaud, G., 2008. FE modelling of bainitic steels using crystal plasticity. Philos. Mag. 88, 3757–3777.

Parisot, R., Forest, S., Gourgues, A.F., Pineau, A., Mareuse, D., 2000. Modeling the mechanical behavior of a multicrystalline zinc coating on a hot-dip galvanized steel sheet. Comput. Mater. Sci. 19, 189–204.

Paula, E., Silva, E., Com-Nougue, J., Beranger, G., Lacombe, P., 1971. Relation entre la cinetique de vieillissement apres deformation du zirconium-α et la diffusion anisotrope de l'oxygene à courte distance. Scr. Metall. 5, 795–800.

Penning, P., 1972. Mathematics of the Portevin-Le Chatelier effect. Acta Metall. 20, 1169–1175.

Pujol, C., Levy, L., Allais, L., 1995. Fluage α-Zr à 200 °C: comportement macroscopique et approche micro-structurale. In: Journée d'Etudes sur le Zirconium. INSTN, Saclay, pp. 13–23.

Quey, R., Dawson, P., Barbe, F., 2011. Large-scale 3D random polycrystals for the finite element method: generation, meshing and remeshing. Comput. Methods Appl. Mech. Eng. 200, 1729–1745.

Raabe, D., Sachtleber, M., Zhao, Z., Roters, F., Zaefferer, S., 2001. Micromechanical and macromechanical effects in grain scale polycrystal plasticity experimentation and simulation. Acta Mater. 49, 3433–3441.

Rosi, F., Perkins, F., 1953. Mechanical properties and strain aging effects in titanium. Trans. Am. Soc. Metals 45, 972–992.

Roth, A., Lebyodkin, M., Lebedkina, T., Lecomte, J.S., Richeton, T., Amouzou, K., 2014. Mechanisms of anisotropy of mechanical properties of α-titanium in tension conditions. Mater. Sci. Eng. A 596, 236–243.

Schoeck, G., Seeger, A., 1959. The flow stress of iron and its dependence on impurities. Acta Metall. 7, 469–477.

Seeger, A., 1956. On the theory of the low-temperature internal friction peak observed in metals. Philos. Mag. 1, 651–662.

Senkov, O., Jonas, J., 1996. Dynamic strain aging and hydrogen-induced softening in α titanium. Metall. Trans. A 27, 1877–1887.

Siska, F., Forest, S.,P.,G., Weygand, D., 2007. Finite element simulations of the cyclic elastoplastic behaviour of copper thin films. Model. Simul. Mater. Sci. Eng. 15, S217–S238.

Snoek, J., 1941. Effect of small quantities of carbon and nitrogen on the elastic and plastic properties of iron. Physica 8, 711–733.

Strudel, J., 1984. Interactions between dislocations and impurities. In: Igata, N., de Fouquet, J. (Eds.), Japan-France Seminar on Fundamental Aspects of Mechanical Properties and Microstructure Evolution of Stainless Steels at High Temperature. University of Tokyo, pp. 169–180.

Taupin, V., Capolungo, L., Fressengeas, C., Das, A., Upadhyay, M., 2013. Grain boundary modeling using an elasto-plastic theory of dislocation and disclination. J. Mech. Phys. Solids 61, 370–384.

Tsukahara, H., Iung, T., 1998. Finite element simulation of the Piobert-Lüders behavior in an uniaxial tensile test. Mater. Sci. Eng. A 248, 304–308.

Tsukahara, H., Iung, T., 1999. Piobert-Lüders and Portevin-Le Chatelier instabilities. Finite element modelling with ABAQUS. J. de Physique IV (9), 157–164.

Veevers, K., Rotsey, W., 1968. Effect of irradiation of strain ageing in annealed Zircaloy-2. J. Nucl. Mat. 27, 108–111.

Veevers, K., Snowden, K., 1973. Strain ageing of quenched Zircaloy-2. J. Nucl. Mat. 47, 311–316.

Wang, H., Berdin, C., Mazière, M., Forest, S., Prioul, C., Parrot, A., Le-Delliou, P., 2012. Experimental and numerical study of dynamic strain ageing and its relation to ductile fracture of a c-mn steel. Mater. Sci. Eng. A 547, 19–31.

Weiss, J., Richeton, T., Louchet, F., Lebyodkin, M., 2007. Evidence for universal intermittent crystal plasticity from acoustic emission and high resolution extensometry. Phys. Rev. B 76, 224110.

Yu, D., Chen, X., Yu, W., Chen, G., 2012. Thermo-viscoplastic modeling incorporating dynamic strain aging effect on the uniaxial behavior of Z2CND18.12N stainless steel. Int. J. Plasticity 37, 119–139.

Yu, Q., Qi, L., Tsuru, T., 2015. Origin of dramatic oxygen solute strengthening effect in titanium. Science 347, 635–639.

Zaefferer, S., 2003. A study of active deformation systems in titanium alloys: dependence on alloy composition and correlation with deformation texture. Mater. Sci. Eng. A 344, 20–30.

Zeghadi, A., Forest, S., Gourgues, A.F., Bouaziz, O., 2007. Ensemble averaging stress–strain fields in polycrystalline aggregates with a constrained surface microstructure–part 2: crystal plasticity. Philos. Mag. 87, 1425–1446.

Zhang, C., Li, H., Eisenlohr, P., Liu, W., Boehlert, C.J., Crimp, M.A., Bieler, T.R., 2015. Effect of realistic 3D microstructure in crystal plasticity finite element analysis of polycrystalline Ti-5Al-2.5Sn. Int. J. Plasticity 69, 21–35.

Zhang, S., McCormick, P., Estrin, Y., 2001. The morphology of Portevin-Le Chatelier bands: finite element simulation for Al-Mg-Si. Acta Mater. 49, 1087–1094.

Zhao, Z., Ramesh, M., Raabe, D., Cuitio, A., Radovitzky, R., 2008. Investigation of three-dimensional aspects of grain-scale plastic surface deformation of an aluminum oligocrystal. Int. J. Plasticity 24, 2278–2297. http://www.sciencedirect.com/science/article/pii/s074964190800020X. http://dx.doi.org/10.1016/j.ijplas.2008.01.002.

Zset Software, 1996. http://www.zset-software.com.